The Astrophysical Journal Letters, 960:L18 (15pp), 2024 January 10 https://doi.org/10.3847/2041-8213/ad16e7

Characterizing the Ordinary Broad-line Type Ic SN 2023pel from the Energetic GRB 230812B

Gokul P. Srinivasaragavan[1,2,3], Vishwajeet Swain[4], Brendan O'Connor[5], Shreya Anand[6], Tomás Ahumada[6], Daniel Perley[7], Robert Stein[6], Jesper Sollerman[8], Christoffer Fremling[6,9], S. Bradley Cenko[2,3], S. Antier[10], Nidhal Guessoum[11], Thomas Hussenot-Desenonges[12], Patrice Hello[12], Stephen Lesage[13,14], Erica Hammerstein[1], M. Coleman Miller[1,2,3,15], Igor Andreoni[1,2,3,27], Varun Bhalerao[4], Joshua S. Bloom[16,17], Anirban Dutta[18], Avishay Gal-Yam[19], K-Ryan Hinds[7], Amruta Jaodand[6], Mansi Kasliwal[6], Harsh Kumar[4,20], Alexander S. Kutyrev[1,3], Fabio Ragosta[21], Vikram Ravi[6], Kritti Sharma[6], Rishabh Singh Teja[18], Sheng Yang[22], G. C. Anupama[18], Eric C. Bellm[23], Michael W. Coughlin[24], Ashish A. Mahabal[6,25], Frank J. Masci[25], Utkarsh Pathak[4], Josiah Purdum[9], Oliver J. Roberts[26], Roger Smith[9], and Avery Wold[25]

[1] Department of Astronomy, University of Maryland, College Park, MD 20742, USA; gsriniv2@umd.edu
[2] Joint Space-Science Institute, University of Maryland, College Park, MD 20742, USA
[3] Astrophysics Science Division, NASA Goddard Space Flight Center, 8800 Greenbelt Road, Greenbelt, MD 20771, USA
[4] Department of Physics, Indian Institute of Technology Bombay, Powai, 400 076, India
[5] McWilliams Center for Cosmology, Department of Physics, Carnegie Mellon University, Pittsburgh, PA 15213, USA
[6] Division of Physics, Mathematics and Astronomy, California Institute of Technology, Pasadena, CA 91125, USA
[7] Astrophysics Research Institute, Liverpool John Moores University, Liverpool Science Park, 146 Brownlow Hill, Liverpool L3 5RF, UK
[8] Department of Astronomy, The Oskar Klein Center, Stockholm University, AlbaNova, SE-10691 Stockholm, Sweden
[9] Caltech Optical Observatories, California Institute of Technology, Pasadena, CA 91125, USA
[10] Observatoire de la Côte d'Azur, Université Côte d'Azur, Boulevard de l'Observatoire, F-06304 Nice, France
[11] Physics Department, American University of Sharjah, Sharjah, UAE
[12] IJCLab, Univ Paris-Saclay, CNRS/IN2P3, Orsay, France
[13] Center for Space Plasma and Aeronomic Research, University of Alabama in Huntsville, Huntsville, AL 35899, USA
[14] University of Alabama in Huntsville, 320 Sparkman Drive, Huntsville, AL 35899, USA
[15] Center for Research and Exploration in Space Science and Technology, NASA/GSFC, Greenbelt, MD 20771, USA
[16] Department of Astronomy, University of California, Berkeley, CA 94720-3411, USA
[17] Lawrence Berkeley National Laboratory, 1 Cyclotron Road, MS 50B-4206, Berkeley, CA 94720, USA
[18] Indian Institute of Astrophysics, 2nd Block 100 Feet Road, Koramangala Bangalore, 560 034, India
[19] Department of Particle Physics and Astrophysics, Weizmann Institute of Science, 76100 Rehovot, Israel
[20] Harvard College Observatory, Harvard University, 60 Garden Street, Cambridge, MA 02158, USA
[21] INAF, Osservatorio Astronomico di Roma, via Frascati 33, I-00078 Monte Porzio Catone (RM), Italy
[22] Henan Academy of Sciences, Zhengzhou 450046, Henan, People's Republic of China
[23] DIRAC Institute, Department of Astronomy, University of Washington, 3910 15th Avenue NE, Seattle, WA 98195, USA
[24] School of Physics and Astronomy, University of Minnesota, Minneapolis, MN 55455, USA
[25] IPAC, California Institute of Technology, 1200 East California Boulevard, Pasadena, CA 91125, USA
[26] Science and Technology Institute, Universities Space and Research Association, 320 Sparkman Drive, Huntsville, AL 35805, USA
Received 2023 October 22; revised 2023 November 17; accepted 2023 December 9; published 2024 January 9

Abstract

We report observations of the optical counterpart of the long gamma-ray burst (GRB) GRB 230812B and its associated supernova (SN) SN 2023pel. The proximity ($z = 0.36$) and high energy ($E_{\gamma,\mathrm{iso}} \sim 10^{53}$ erg) make it an important event to study as a probe of the connection between massive star core collapse and relativistic jet formation. With a phenomenological power-law model for the optical afterglow, we find a late-time flattening consistent with the presence of an associated SN. SN 2023pel has an absolute peak r-band magnitude of $M_r = -19.46 \pm 0.18$ mag (about as bright as SN 1998bw) and evolves on quicker timescales. Using a radioactive heating model, we derive a nickel mass powering the SN of $M_{\mathrm{Ni}} = 0.38 \pm 0.01\,M_\odot$ and a peak bolometric luminosity of $L_{\mathrm{bol}} \sim 1.3 \times 10^{43}$ erg s^{-1}. We confirm SN 2023pel's classification as a broad-line Type Ic SN with a spectrum taken 15.5 days after its peak in the r band and derive a photospheric expansion velocity of $v_{\mathrm{ph}} = 11{,}300 \pm 1600$ km s^{-1} at that phase. Extrapolating this velocity to the time of maximum light, we derive the ejecta mass $M_{\mathrm{ej}} = 1.0 \pm 0.6\,M_\odot$ and kinetic energy $E_{\mathrm{KE}} = 1.3^{+3.3}_{-1.2} \times 10^{51}$ erg. We find that GRB 230812B/SN 2023pel has SN properties that are mostly consistent with the overall GRB-SN population. The lack of correlations found in the GRB-SN population between SN brightness and $E_{\gamma,\mathrm{iso}}$ for their associated GRBs across a broad range of 7 orders of magnitude provides further evidence that the central engine powering the relativistic ejecta is not coupled to the SN powering mechanism in GRB-SN systems.

[27] Gehrels Fellow.

Unified Astronomy Thesaurus concepts: Gamma-ray bursts (629); Core-collapse supernovae (304); Relativistic jets (1390)

1. Introduction

A clear link has been established over the past two decades between long-duration gamma-ray bursts (LGRBs; $T_{90} > 2$ s) and core-collapse supernovae on an observational basis (Woosley & Bloom 2006). Photometrically, a characteristic supernova (SN) "bump" arises in the afterglow light curve (LC) within 10–20 days, as the afterglow fades. Over 40 LGRBs with this characteristic bump have been discovered (see, e.g., Hjorth 2013; Cano et al. 2017a; Melandri et al. 2019; Hu et al. 2021; Kumar et al. 2022a; Rossi et al. 2022; Blanchard et al. 2023; Srinivasaragavan et al. 2023) and are known as GRB-SNe. Spectroscopic observations of these SNe have revealed that almost all (SN 2011kl associated with GRB 111209A was a superluminous SN; Greiner et al. 2015; Kann et al. 2019) are broad-line Type Ic SNe (Type Ic-BL; Woosley & Bloom 2006); they lack hydrogen and helium lines in their optical spectra and have broad lines corresponding to ejecta velocities higher than those seen in normal Type Ic explosions. Before this work, 28 GRB-SNe had been spectroscopically confirmed (see, e.g., Cano et al. 2017a, 2017b; Wang et al. 2018; Melandri et al. 2019; Hu et al. 2021; Kumar et al. 2022a; Rossi et al. 2022; Blanchard et al. 2023).

However, there remain a number of open questions surrounding the GRB-SN connection, and recent discoveries have shown that our understanding of the connection may not be as complete as once thought. An SN is not always detected for nearby LGRBs (Della Valle et al. 2006; Fynbo et al. 2006; Gal-Yam et al. 2006; Tanga et al. 2018), and the physical link between LGRBs and their associated SN is also not clear. Studies of the brightest GRB of all time, GRB 221009A (Frederiks et al. 2023a; Lesage et al. 2023b; Burns et al. 2023; Kann et al. 2023; Laskar et al. 2023; LHAASO Collaboration et al. 2023; Malesani et al. 2023; O'Connor et al. 2023; Williams et al. 2023), have shown that its associated SN has a peak luminosity consistent with those of the rest of the GRB-SN population (Levan et al. 2023b; Blanchard et al. 2023; Fulton et al. 2023; Kann et al. 2023; Shrestha et al. 2023; Srinivasaragavan et al. 2023), despite the GRB being more luminous by orders of magnitude. On the other hand, SN 1998bw associated with GRB 0980425 was a very nearby ($z = 0.0085$; Iwamoto et al. 1998; Patat et al. 2001; Clocchiatti et al. 2011) and relatively luminous SN with a derived nickel mass ($M_{\rm Ni}$) powering the SN as high as 0.9 $M_\odot$ (Sollerman et al. 2000). Its associated GRB 980425 was a low-luminosity GRB with an isotropic equivalent energy of $E_{\gamma,\rm iso} \sim 10^{48}$ erg (Galama et al. 1998), which is 3–4 orders of magnitude fainter than what is seen for cosmological GRBs. Numerous observational studies have also been done on GRB-SNe whose associated GRBs have energies in between GRB 221009A and GRB 0908425 (see, e.g., Matheson et al. 2003; Malesani et al. 2004; Mazzali et al. 2006; Starling et al. 2011; Schulze et al. 2014), and they paint a scattered picture regarding the relationship between GRB energetics and SN properties.

The origin and classification of LGRBs based solely on their T_{90} has also come into question, as GRB 211211A ($T_{90} \sim 34.3$ s; Mangan et al. 2021) and GRB 230307A ($T_{90} \sim 35$ s; Dalessi et al. 2023) may have had associated kilonova emission, pointing toward a compact object origin (Rastinejad et al. 2022; Troja et al. 2022; Yang et al. 2022; Levan et al. 2023a; Gillanders et al. 2023; Yang et al. 2023). Studies of the LGRBs' surrounding interstellar medium (ISM) also show evidence for LGRBs that do not arise from the collapse of massive stars, but rather compact object mergers (Leśniewska et al. 2022). Therefore, it is important to follow up nearby, bright LGRBs and their associated SNe across the electromagnetic spectrum in order to shed light on some of these questions surrounding the GRB-SN connection. Here we report on the characterization of one such GRB-SN.

GRB 230812B was discovered by the Fermi Gamma-Ray Burst Monitor (GBM; Meegan et al. 2009) at 18:58:12 UTC on 2023 August 12, which we establish hereafter as T_0 (Lesage et al. 2023a). The burst has a $T_{90} = 2.95 \pm 1.02$ s (Roberts et al. 2023) and a fluence of $2.69 \pm 0.01 \times 10^{-4}$ erg cm^{-2} in the 10–1000 keV band. The afterglow was subsequently detected as an X-ray point source by the Swift X-Ray Telescope (XRT; Burrows et al. 2005) at $T_0 + 0.297$ days (Beardmore et al. 2023). Its brightness prompted follow-up across the electromagnetic spectrum (Lipunov et al. 2023a, 2023b; Salgundi et al. 2023; Zheng et al. 2023); and the optical counterpart was discovered by Zheng et al. (2023) and Salgundi et al. (2023). Spectroscopic observations of the optical afterglow led to a redshift measurement of $z = 0.36$ (de Ugarte Postigo et al. 2023). At this redshift, using a flat ΛCDM cosmology with $\Omega_{\rm m} = 0.286$ and $H_0 = 69.6$ km s^{-1} Mpc^{-1} to convert redshifts to distances, the burst has an isotropic equivalent energy release of $E_{\gamma,\rm iso} \sim 1.1 \times 10^{53}$ erg. Using the T_{90} reported, the burst has an isotropic equivalent average gamma-ray luminosity of $L_{\gamma,\rm iso} \sim 8.8 \times 10^{52}$ erg s^{-1}. Comparing these values to the LGRB population with observationally confirmed SNe, GRB 230812B possesses the fifth-highest $E_{\gamma,\rm iso}$ and second-highest $L_{\gamma,\rm iso}$. This makes GRB 230812B a rare example of an energetic LGRB nearby enough to search for an associated Type Ic-BL SN.

In this Letter, we present optical observations of the afterglow of GRB 230812B that display a clear late-time flattening consistent with an associated SN (SN 2023pel; Agui Fernandez et al. 2023) and spectroscopic observations confirming SN 2023pel as a Type Ic-BL SN. In Section 2, we report our observations of the optical counterpart; in Section 3, we analyze the optical counterpart and find its associated SN 2023pel; in Section 4, we analyze SN 2023pel and characterize its key properties; and in Section 5, we summarize our conclusions. We report the photometry obtained of GRB 230812B/SN 2023pel in Table 1 in the Appendix. Hussenot-Desenonges et al. (2023) also report an analysis of this event, and, where relevant, we compare our results with theirs.

2. Observations

2.1. Swift

Observations of the afterglow with the Neil Gehrels Swift Observatory (Gehrels et al. 2004) XRT began at $T_0 + 25$ ks (Beardmore et al. 2023), localizing the afterglow of the GRB. The data were obtained in Photon Counting (PC) mode. We retrieved the time-averaged XRT PC mode spectrum from the Swift-XRT GRB Lightcurve Repository[28] (Evans et al. 2009). The spectrum contains 5.0 ks of data obtained between $T_0 + 25$

[28] https://www.swift.ac.uk/xrt_curves/

and $T_0 + 38$ ks, with a midtime of $T_0 + 8.8$ hr. The data are grouped into a minimum of 1 count bin^{-1}. We also retrieve the X-ray LC, which contains data obtained between $T_0 + 25$ and $T_0 + 1421$ ks.

We likewise retrieved the data obtained by the Ultra-Violet/Optical Telescope (UVOT; Roming et al. 2005) from the Swift Data Archive.[29] All observations were obtained using the broadband white filter (hereafter wh). We focused on the initial wh-filter data (ObsID: 00021619001) with a total exposure of 4881 s. The data were combined using the `uvotimsum` task within `HEASoft v6.29c` (Nasa High Energy Astrophysics Science Archive Research Center (Heasarc), 2014). Due to an issue with the Swift gyroscope affecting attitude control (Cenko 2023), the image point-spread function (PSF) is elongated. We therefore utilized a lenticular source region with a position angle of 302° to match the shape of the PSF and selected two nearby, source-free circular regions of 15″ radius as background. We used the `uvotsource` and `uvot2pha` tasks to measure the photometry and retrieve the spectral files. At this epoch, we measure a source brightness of wh $= 19.29 \pm 0.06$ AB mag. We obtain similar results (consistent within 1σ errors) using `uvotdetect`, which automatically selects the source region. Therefore, we conclude that our treatment of the elongated PSF is reasonable.

2.2. Zwicky Transient Facility

The Zwicky Transient Facility (ZTF; Bellm et al. 2019; Graham et al. 2019; Masci et al. 2019; Dekany et al. 2020) is a public–private survey that images the entire northern sky every 2 days in the g and r bands. The transient detection with ZTF relies on image subtraction, using templates of predefined fields. Any high-significance difference ($>5\sigma$) generates an alert containing information about the transient (Patterson et al. 2019). We query the alert stream via Kowalski (Duev et al. 2019) through an alert filtering scheme on Fritz previously described in short-duration GRB and gravitational-wave searches (Kasliwal et al. 2020; Ahumada et al. 2021, 2022). In a nutshell, we select sources that are spatially and temporally consistent with the GBM localization, far from Panoramic Survey Telescope and Rapid Response System 1 (PS1) stars (based on Tachibana & Miller 2018) or bright sources, and real based on the real–bogus score (Duev et al. 2019), as well as those that have a positive residual and at least two detections separated by a minimum of 15 minutes.

We ingested the GBM localization map (Goldstein et al. 2022) into Fritz (van der Walt et al. 2019), the ZTF instance of SkyPortal (van der Walt et al. 2019; Coughlin et al. 2023), an interactive tool designed to plan and schedule target-of-opportunity observations for ZTF. The observing plan was generated using `gwemopt` (Coughlin et al. 2019) by taking the healpix Fermi-GBM localization map, slicing the sky map into predefined tiles of the size and shape of the ZTF field of view, determining which fields have the highest enclosed probability, and optimizing observations based on air mass and visibility windows. For this purpose, we used a modified version of the greedy algorithm (Coughlin et al. 2018; Almualla et al. 2020), only allowing for the use of the ZTF primary grid. The final schedule consisted of 300 s exposures in the r and g bands starting 8.6 hr after the GBM detection. The observing plan for the first night covered 420 deg^2 beginning at 2023 August 13 03:34:57 using three epochs of nine fields totaling 2.25 hr. This corresponds to 78% of the probability enclosed in the Earth occultation–corrected GRB localization map. The exposures reached median depths of 21.9 mag in both the g and r bands (Salgundi et al. 2023). The first ZTF detection of the afterglow ZTF 23aaxeacr happened 8.61 hr after the burst, during the first ZTF exposure of the field, as the transient was sitting in the ZTF field that covered the highest probability.

For GRB 230812B, ZTF detected 22,154 sources in the GBM error region in difference imaging, though only 55 sources passed our filtering criteria. These sources were cross-matched against the Wide-field Infrared Survey Explorer (Cutri et al. 2013), milliquas (Flesch 2019), and the Minor Planet Center to ensure that they were not active galactic nuclei (Stern et al. 2012) or solar system objects. Finally, we queried the IPAC-ZTF forced-photometry service using a monthlong baseline to reject young SNe. The majority of the candidates were ruled out by one (or multiple) of the criteria previously described. The afterglow of GRB 230812B, ZTF23 aaxeacr/SN 2023pel (α (J2000) $= 16^{\rm h}36^{\rm m}31\overset{\rm s}{.}48$, δ (J2000) $= +47°51'32\overset{''}{.}26$; Salgundi et al. 2023), was found during the first night of observations due to the fast evolution of 2 mag day^{-1} shown in the r-band ZTF data. No other candidate showed a photometric evolution consistent with an afterglow, and the source was reported to the Transient Name Server (AT 2023pel; Salgundi et al. 2023) once its fast evolution was confirmed. Our report came only 4 minutes after the refined Swift XRT localization, and our source was consistent (within 6″) with the center of the XRT region (Page & Swift-XRT Team 2023).

2.3. Spectral Energy Distribution Machine

Once the afterglow was identified, we used the Rainbow Camera on the Spectral Energy Distribution Machine (SEDM; Blagorodnova et al. 2018; Rigault et al. 2019) mounted on the Palomar 60 inch telescope to acquire u-, g-, r-, and i-band imaging in 300 s exposures. The SEDM images started 11.02 hr after the burst. The SEDM images were processed with a `Python`-based pipeline version of `Fpipe` (Fremling et al. 2016), which includes photometric calibrations and image subtraction using reference images from the Sloan Digital Sky Survey (Abazajian et al. 2009).

2.4. Liverpool Telescope

The location of the GRB was observed with IO:O, the optical imager on the 2 m robotic Liverpool Telescope (LT; Steele et al. 2004) at the Observatorio del Roque de los Muchachos. Observations were taken on three separate nights: 2023 August 14 (*griz* filters), 2023 August 16 (*gri*), and 2023 September 4 (*r*).

Reduced images were downloaded from the LT archive and processed with custom image subtraction and analysis software (K. Hinds and K. Taggart et al. 2023, in preparation). Image stacking and alignment is performed using SWarp (Bertin 2010) where required. Image subtraction is performed using a preexplosion reference image in the appropriate filter from PS1 (Flewelling et al. 2020). The photometry is measured using PSF fitting methodology relative to PS1 standards and based on techniques in Fremling et al. (2016).

[29] https://heasarc.gsfc.nasa.gov/cgi-bin/W3Browse/swift.pl

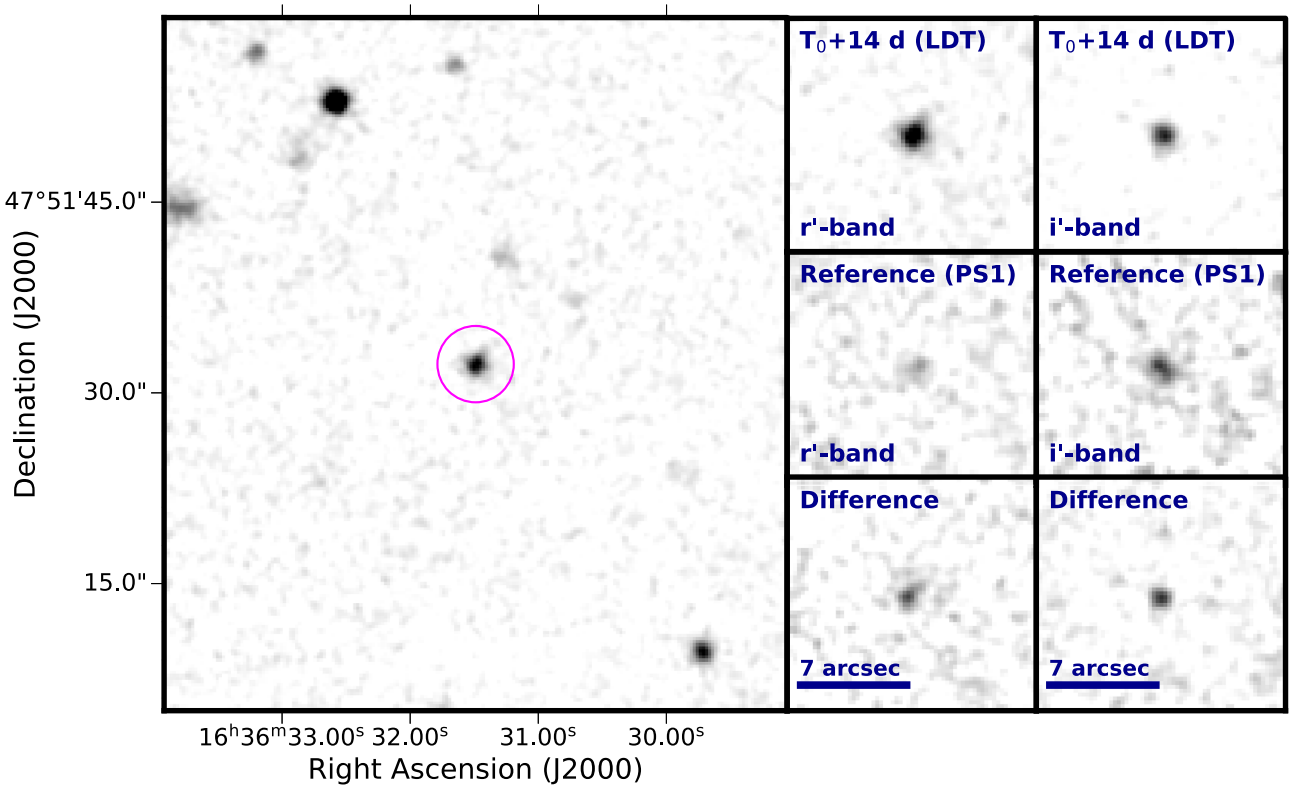

Figure 1. LDT images of the optical afterglow of GRB 230812B/SN 2023pel. The large left panel shows the wider field of view of GRB 230812B in the *r* band 14 days after T_0. The right panels show the observations taken of the GRB that include the host galaxy contribution, the reference images from PS1 used for image subtraction, and the resulting subtracted images used for photometry in both the *r* and *i* bands. The images have been smoothed for display purposes.

2.5. Lowell Discovery Telescope

We also observed GRB 230812B's optical counterpart in *r* and *i* with the 4.3 m Large Monolithic Imager on the Lowell Discovery Telescope (LDT) for five epochs between UT 2023 August 26 and 2023 September 9. We reduced the images using a custom `Python`-based image analysis pipeline (Toy et al. 2016) that performs data reduction, astrometry, registration, source extraction, and PSF photometry using `SExtractor` (Bertin & Arnouts 1996). `SExtractor` was calibrated using point sources from the PS1 DR1 catalog. We then performed image subtraction using the PS1 templates and the `ZOGY` algorithm-based `Python` pipeline (Zackay et al. 2016; Kumar et al. 2022a) to remove the host contribution. Figure 1 shows both the wider field of view of GRB 230812B's position on the sky and its flux in both filters at $T_0 + 14$ days.

2.6. GROWTH-India Telescope

We used the 0.7 m GROWTH-India Telescope (GIT; Kumar et al. 2022b) located at the Indian Astronomical Observatory (IAO), Hanle-Ladakh, to acquire data of GRB 230812B's optical counterpart. The counterpart was observed in the Sloan g', r', and i' bands starting 20 hr after T_0. We continued observations for up to 7 days by acquiring multiple 300 s exposures. The data were downloaded and processed in real time by the GIT data reduction pipeline (Kumar et al. 2022c). We used individual exposures of 300 s for photometry in the early stages when the afterglow was bright. Later, we stacked images with `SWarp` (Bertin 2010) to increase the signal-to-noise ratio of the detections.

All images were preprocessed by subtracting bias images, flat-fielding, and removing cosmic rays via the Astro-SCRAPPY (McCully & Tewes 2019) package. Astrometry was performed on the resulting images using the offline `solve-field` (Lang et al. 2010) astrometry engine. Subsequently, refined astrometry was conducted using the `SCAMP` (Bertin 2006) package to facilitate image stacking with `SWarp` (Bertin 2010). Sources were detected using `SExtractor` (Bertin & Arnouts 1996) and crossed-matched against the PS1 DR1 catalog (Chambers et al. 2016) through Vizier to obtain the zero-point in the images. Using the `ZOGY` algorithm-based `Python` pipeline, we performed image subtraction on all images using the PS1 templates. Finally, the pipeline performed PSF fit photometry on the subtracted images to obtain magnitudes.

2.7. Himalayan Chandra Telescope

The 2 m Himalayan Chandra Telescope (HCT) situated at the IAO in Hanle-Ladakh was used to observe the optical counterpart of GRB 230812B. This counterpart was observed in the Sloan r' and i' bands beginning 3 days after T_0. During the period of UT 2023 August 15 to 2023 August 24, we conducted four observations, capturing multiple exposures lasting between 20 and 40 minutes each. Standard image reduction techniques were applied, including bias subtraction and flat-fielding, as well as cosmic-ray removal using the Astro-SCRAPPY package. Astrometry was conducted on the resulting images using the offline `solve-field` astrometry engine. We then used the same methods as in Section 2.6 to extract sources, perform image subtraction, and perform PSF photometry to get the magnitudes of the GRB counterpart.

2.8. Keck

We obtained a spectrum of GRB 230812B/SN 2023pel on UT 2023 September 9 05:31:47 using the Deep Imaging Multi-Object Spectrograph (DEIMOS; Faber et al. 2003) mounted on the 10 m Keck II telescope. Our configuration used a 600ZD grating, a central wavelength of 7500 Å, and the OG 550 filter to maximize redder wavelength coverage. The observation consisted of 3×1800 s exposures and one 900 s exposure totaling 1.75 hr. The data were calibrated and reduced using `Pypeit` (Prochaska et al. 2020).

3. Afterglow Analysis

3.1. Characterization of X-Ray and Optical Afterglow

We start with determining some of the basic afterglow properties and note that an in-depth, multiwavelength study of the afterglow is forthcoming in U. P. Pathak et al. (2023, in preparation). We find that the power-law temporal decay indices of the X-ray (Swift XRT) and optical data (using the g, r, and i bands prior to when the SN emission affects the LC, $<T_0+4$ days), are consistent, with $\alpha_X = 1.31^{+0.07}_{-0.06}$ ($\chi^2_{\rm reduced} = 0.96$) and $\alpha_O = 1.31 \pm 0.02$ ($\chi^2_{\rm reduced} = 2.14$). We then calculate the spectral index in the optical using SEDM observations in the u, g, r, and i bands from SEDM at $T_0 + 10.8$ hr. We derive $\beta_O = 0.74 \pm 0.02$ ($\chi^2_{\rm reduced} = 0.76$) after correcting for line-of-sight extinction through the Galactic plane ($A_V = 0.06$ mag; Schlafly & Finkbeiner 2011). These values are consistent with the results of Hussenot-Desenonges et al. (2023), who find $\alpha_O = 1.35 \pm 0.02$ and $\beta_O = 0.74 \pm 0.01$.

We then perform an X-ray analysis through `XSPEC v12.12.0` using the initial PC mode XRT spectrum. We modeled the spectrum assuming an absorbed power-law model `tbabs*ztbabs*pow`, which is a Tuebingen–Boulder ISM absorption model that calculates the cross section for X-ray absorption by the ISM (Wilms et al. 2000). We fix the Galactic hydrogen column density to $N_{\rm H,MW} = 2.0 \times 10^{20}$ cm^{-2} (Willingale et al. 2013) and a redshift of $z = 0.36$. We fit the data by minimizing the Cash statistics (Cash 1979). We obtain a best-fit (C-stat = 259 for 332 degrees of freedom, dof) X-ray photon index of $\Gamma_{\rm X} = 1.765 \pm 0.085$ and intrinsic hydrogen column density $N_{{\rm H},z} = (1.2 \pm 0.4) \times 10^{21}$ cm^{-2}. This corresponds to an X-ray spectral index of $\beta_{\rm X} = \Gamma_{\rm X} - 1 = 0.765 \pm 0.085$. The consistency between the optical and X-ray spectral indices suggests that the optical and X-ray data lie on the same spectral segment (see Figure 2).

Therefore, we include the early optical data (u, g, r, and i filters) obtained by SEDM, each shifted to a midtime of 8.8 hr using the best-fit temporal power law, to constrain the possibility of dust intrinsic to the GRB environment through modeling the broadband spectral energy distribution (SED) again in `XSPEC v12.12.0`. We fix the Milky Way dust reddening to $E(B-V)_{\rm MW} = 0.02$ mag (Schlafly & Finkbeiner 2011). The broadband SED was fit using the model `tbabs*ztbabs*redden*zdust*pow`, which again uses the Tuebingen–Boulder ISM absorption model to account for absorption and extinction in both the Milky Way and the host galaxy. We applied a Milky Way extinction law with $R_V = 3.1$ (Cardelli et al. 1989) and derive a photon index of $\Gamma_{\rm XO} = 1.73 \pm 0.02$, $N_{{\rm H},z} = (1.1 \pm 0.2) \times 10^{21}$ cm^{-2}, and $E(B-V)_z < 0.07$ mag (3σ) for a $\chi^2 = 363$ for 336 dof. This is consistent with the results of Hussenot-Desenonges et al. (2023), who find $E(B-V)_z < 0.03$ mag. We show the broadband modeling described, along with the X-ray and optical data, at a midtime of $T_0 + 8.8$ hr in Figure 2. Given the low upper limit derived, we ignore the host galaxy extinction for the rest of our analysis.

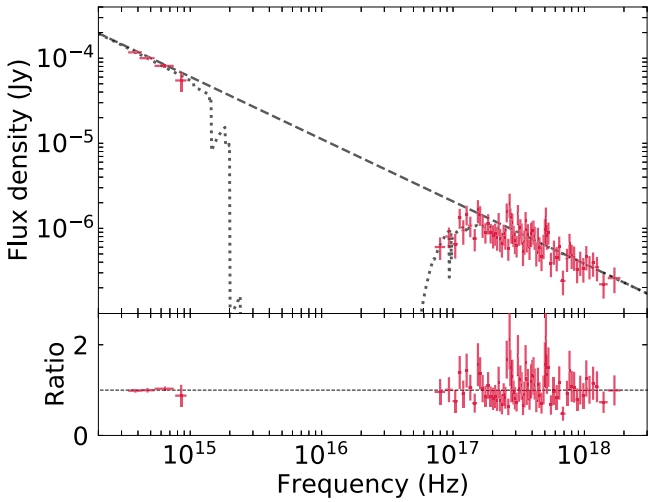

Figure 2. Broadband modeling of the GRB afterglow from optical (ZTF and SEDM; *ugri*) to X-ray (Swift) wavelengths at a midtime of $T_0 + 8.8$ hr. The model is a simple absorbed power law shown by the gray dotted line, and the unabsorbed model is shown as the gray dashed line, both corrected for Galactic extinction. The bottom panel shows the ratio between the data and the absorbed power-law model, with the black dashed line showing a ratio of unity.

The spectral index we derive ($\beta_{\rm OX} = 0.73 \pm 0.02$) does not match with a locally fast-cooling environment ($\nu_m < \nu_c < \nu$, where ν_m is the injection frequency of the electrons and ν_c is the cooling frequency), as the slope of the electron energy distribution p would be abnormally low (1.46 ± 0.04), according to the standard closure relations (Sari et al. 1998; Granot & Sari 2002). Instead, a more reasonable value of $p = 2.46 \pm 0.04$ is obtained for $\nu_m < \nu < \nu_c$, assuming an adiabatic jet and constant density ISM. This points toward a slow-cooling regime for the synchrotron afterglow in the optical to X-ray bands (see Pathak et al. 2023, in preparation, for more details).

3.2. SN Bump

A clear late-time flattening is seen as soon as $T_0 + 7$ days in Figure 3 in both the r and i bands, which we interpret as due to rising SN emission. Kann et al. (2007) and Oates et al. (2009) have shown that if the central engine is still active, a rebrightening of the optical afterglow may occur shortly after the prompt emission. Greiner et al. (2009) has also shown that optical flaring due to refreshed or reversed shocks can cause brightening episodes in the early-time optical afterglow LC. However, the X-ray LC of GRB 230812B (see Figure 5) shows no evidence of flaring at early times and does not rebrighten when the optical afterglow begins to, which occurs a week after the prompt emission. Therefore, we determine that the late-time flattening cannot be explained by central engine activity.

It has been shown that LGRBs 211211A and 230307A have evidence of associated kilonova emission (Rastinejad et al. 2022; Troja et al. 2022; Yang et al. 2022; Levan et al. 2023a). In order to determine if the late-time flattening could be due to a kilonova, we transform the kilonova LC associated with GRB 130603B (Berger et al. 2013) to the redshift of GRB 230812B ($z = 0.36$) and apply the line-of-sight Galactic extinction. We find that the kilonova peaks around 26 mag in the H band and therefore would be even fainter in the optical bands. This is too

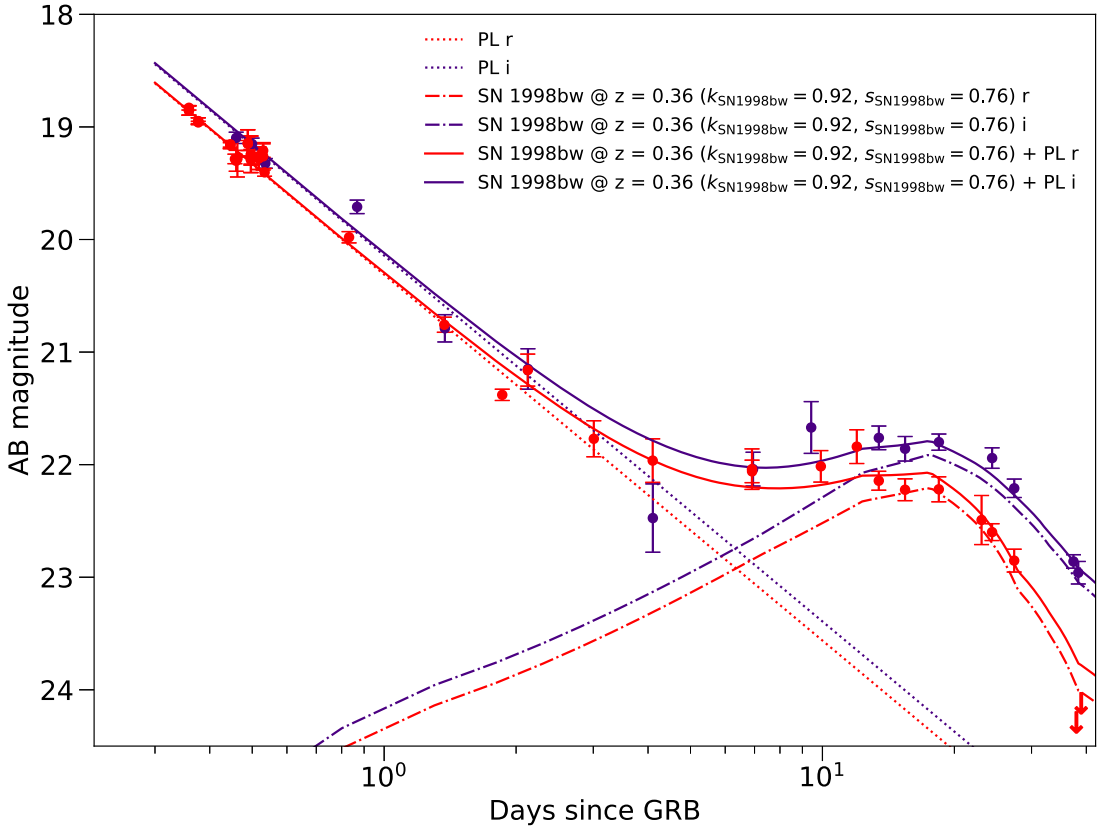

Figure 3. Observed *r*- and *i*-band photometry of GRB 230812B from the optical instruments listed in Section 2, with all magnitudes already host galaxy–subtracted. The photometry values are reported in Table 1, and all times are in the observer frame. We also show the best-fit power-law decay to the optical data derived in Section 3.1, corresponding to a power-law decay index of $\alpha = 1.31$. The LCs for an SN 1998bw–like source in the *r* and *i* bands, redshifted to $z = 0.36$, reddened according to the line-of-sight Galactic extinction of GRB 230812B, with a flux-stretching factor of $k = 0.92$ and time-stretching factor of $s = 0.76$ (derived in Section 3.2) applied, are also shown.

faint to cause any significant late-time flattening in the optical afterglow LC, which leads us to determine that the late-time flattening cannot be explained by an associated kilonova.

Therefore, the most likely explanation for the late-time flattening is an associated SN. In order to compare the associated SN to SN 1998bw (the prototypical SN associated with a GRB used in modeling studies due to the proximity of the SN at $z = 0.0085$), we use the `PyMultiNest` Bayesian modeling package (Feroz et al. 2009; Buchner et al. 2014) to find the best-fit flux-stretching factor ($k_{SN1998bw}$) and time-stretching factor ($s_{SN1998bw}$) of the SN with respect to SN 1998bw. The full model that we use is

$$f_\nu(t_{obs}) = k_{SN1998bw}(f_\nu^{SN1998bw}(t_{obs}/s_{SN\ 1998bw})) + a_{AG}(t_{obs})^{-\alpha}, \quad (1)$$

where $f_\nu^{SN1998bw}(t_{obs})$ is the flux seen of SN 1998bw at $z = 0.36$ at a time in the observer frame, t_{obs} is the time in the observer frame, α is the power-law decay index, and a_{AG} is the flux constant of proportionality. We derive $f_\nu^{SN1998bw}$ by (de) reddening and *k*-correcting the nugent-hyper model (Levan et al. 2005) in `SNCosmo` (Barbary et al. 2016) to match the relevant properties of GRB 230812B. We perform the fitting concurrently in the *r* and *i* bands, fixing $\alpha = 1.31$ and a_{AG} (derived in Section 3.1). Therefore, the free parameters in our corresponding fitting procedure are $k_{SN1998bw}$ and $s_{SN1998bw}$. Because a possible correlation may exist between these two parameters (Cano 2014), we create priors for both of the parameters drawn from a bivariate normal distribution fit to the $k_{SN1998bw}$ and $s_{SN1998bw}$ values derived for GRB-SNe in the literature (Cano et al. 2017a). Furthermore, in order to account for systematic uncertainties due to combining data from multiple telescopes (*s*-corrections; Stritzinger et al. 2002), we numerically optimize the likelihood function assuming that the reported errors actually underestimate the true uncertainty. We do this using the same method as Srinivasaragavan et al. (2023), by introducing an error-stretching factor β in the fitting procedure to represent the *s*-correction.

We find that the best-fit values for the flux- and time-stretching factors are $k_{SN1998bw} = 0.92$ and $s_{SN1998bw} = 0.76$, with median $\pm 1\sigma$ values of $k_{SN1998bw} = 0.93^{+0.04}_{-0.03}$ and $s_{SN1998bw} = 0.76 \pm 0.02$. The reduced chi-squared statistic is $\chi^2_{reduced} = 1.2$, indicative that the model is an adequate fit to the observed data. Our $k_{SN1998bw}$ is consistent with the value found by Hussenot-Desenonges et al. (2023) of $k_{SN1998bw} = 1.04 \pm 0.09$, and our $s_{SN1998bw}$ is consistent at the 2σ level with their $s_{SN1998bw} = 0.68 \pm 0.05$. Therefore, we find that the SN associated with GRB 230812B, SN 2023pel, is about as bright as SN 1998bw but evolves on a quicker timescale. We will revisit this when we model the SN parameters in Section 4.2. We note that the presence of a jet break in the optical LC is a possible source of systematic error for this analysis; however, the lack of a jet break in the X-ray LC and our well-sampled optical data set make this an unlikely possibility.

After subtracting the best-fit power-law value from the brightest *r*-band photometry point seen in the late-time

flattening and correcting for the Galactic extinction, we find that the observed peak absolute magnitude of SN 2023pel is $M_r = -19.46 \pm 0.18$ mag, which is consistent with the peak magnitude found in Hussenot-Desenonges et al. (2023), $M_r = -19.41 \pm 0.10$. As expected from the flux-stretching factor we derived, this is consistent with the peak absolute magnitude of SN 1998bw, $M_R = -19.36 \pm 0.05$ mag (Galama et al. 1998), and brighter than what is seen for the the overall Type Ic-BL SN population ($M_r = -18.6 \pm 0.5$ mag; Taddia et al. 2019). We confirm that SN 2023pel is indeed a Type Ic-BL SN in Section 3.3.

3.3. Spectrum Analysis

As described in Section 2.8, we obtained a DEIMOS spectrum on UT 2023 September 9 05:31:47 of GRB 230812B/SN 2023pel, and we show the observed, reduced spectrum after correcting for telluric features in gray in the top panel of Figure 4. Hβ, Hα, and [O III] galaxy emission lines are clearly seen in the spectrum, and we use PYSPECKIT's SPLOT interactive fitting routine (Ginsburg & Mirocha 2011; Ginsburg et al. 2022) to fit these lines to a redshift. We find $z = 0.36112 \pm 0.00004$ (where the error is the rms error), providing an independent confirmation of the redshift of GRB 230812B/SN 2023pel.

We then use the Next Generation Super Fitter (NGSF; Goldwasser et al. 2022) to model the SN and host together. For this, we allow NGSF to explore all available SN and galaxy templates while fixing the value for the redshift and limiting the SN phase to a window between 5 and 25 days after peak. The results show that the NGSF best fit is to an elliptical galaxy with an SN Ic-BL ($\chi^2/\mathrm{dof} \sim 7.45$). However, elliptical hosts for LGRBs are extremely rare, as they usually originate from active star-forming galaxies. So far, GRB 050219A is the only example of an LGRB found in an elliptical (Rossi et al. 2014) galaxy, and the presence of narrow emission lines at the redshift of the host leads us to conclude that the host is most likely not an elliptical galaxy. Therefore, we use the next-best fit with an SN Ic-BL, an S0 spiral galaxy ($\chi^2/\mathrm{dof} \sim 9.80$), to represent the host contribution. We note that NGSF does not include nebular emission in their galaxy templates, though we mask the galaxy lines before performing the fits. When redoing the analysis using the elliptical galaxy template, all of our derived results were consistent within the error bars. The particular template used does not seem to significantly impact our analysis.

We scale the host contribution to the spectrum to the same percentage (44%) of the host contribution to the r-band photometry of GRB 230812B's optical counterpart at the time closest to the spectrum ($T_0 + 27.394$ days), derived from comparing the LDT magnitudes before and after image subtraction. We show the template in brown in the top panel Figure 4 and subtract this template from the observed spectrum. We also subtract the afterglow's spectral model, corresponding to $F_\nu \propto \nu^{-\beta_O}$, where $\beta_O = 0.74$ is the optical spectral index derived in Section 3.1, from the observed spectrum. We scale the spectral model of the afterglow to the same percentage (14%) of the afterglow's contribution to the observed r-band photometry at the time of the spectrum through using the best-fit temporal power law derived in Section 3.1. We show the spectral model in pink in the top panel of Figure 4.

The final host- and afterglow-subtracted, smoothed, and normalized spectrum of SN 2023pel is shown in black in the top panel of Figure 4. The phase of the spectrum corresponds to 15.5 days after the observed peak in the r band. We then use the IDL routine WOMBAT to remove the galaxy emission lines and show that spectrum in the bottom panel of Figure 4. The spectrum shows clear broad absorption features characteristic of Type Ic-BL SNe, confirming the classification from Agui Fernandez et al. (2023). We indicate the Fe II and Si II features in the figure. We then run the SN identification code (SNID; Blondin & Tonry 2007) to determine the best-matched Ic-BL templates. We find that the templates for SN 2002ap, 13 days after its peak, and SN 1998bw, 28 days after its peak, are good matches to the spectrum. As mentioned in Section 3.2, we determined that SN 2023pel evolves on a quicker timescale than SN 1998bw. This agrees with the best-fit SN 1998bw template SNID found, as the matching template has a phase 13 days later than the observed phase of the spectrum of SN 2023pel. We show the observed spectra of SN 2002ap (Mazzali et al. 2002) and SN 1998bw (Patat et al. 2001) at the time of these best-fit templates in pink and green in the bottom panel of Figure 4.

4. SN Analysis

After showing evidence that an SN is the source of the late-time flattening of the afterglow LC, we shift our focus to the analysis of the SN itself. In this section, we investigate whether the SN can be powered by a millisecond magnetar (Section 4.1) or if the observed data are better described by the conventional Arnett (1982) radioactive decay model (Section 4.2) and report progenitor and SN properties corresponding to the respective models. We then analyze a spectrum taken of GRB 230812B/SN 2023pel (Section 3.3) and end by comparing the properties of GRB 230812B/SN 2023pel to those of the rest of the GRB-SN population (Section 4.3).

4.1. Magnetar Model

Although the Arnett (1982) radioactive heating model (see Section 4.2) is the frequently adopted model used to describe Type Ic-BL LCs, theories have shown that a millisecond magnetar central engine can power LGRBs (Usov 1992), and observational studies of multiple GRB-SNe have suggested evidence for a magnetar origin (Toma et al. 2007; Greiner et al. 2015; Cano et al. 2016; Lü et al. 2018; Zhang et al. 2022). We investigate whether our observed X-ray and optical LCs can be explained within the context of this model using the formulation from Cano et al. (2016) before using the Arnett (1982) model. The millisecond magnetar model consists of three phases: an afterglow component whose emission is due to the GRB ejecta colliding with the surrounding medium, a component whose emission is due to the powering of the central engine, and the SN component, whose emission is also due to the powering of the central engine. The X-ray LC is described by just the first two phases, as the SN emission is not significant in the X-ray bandpasses, while the optical LC is described by the addition of all three phases. In order for this model to be viable, the initial magnetic field strength (B_0) and spin period (P_0) derived from the X-ray and optical LC analysis must be consistent with each other. We note that this model assumes that the magnetic field is dipolar in nature and unevolving over time. Therefore, there are no considerations for multipolar and rapidly evolving magnetic fields within the context of this model.

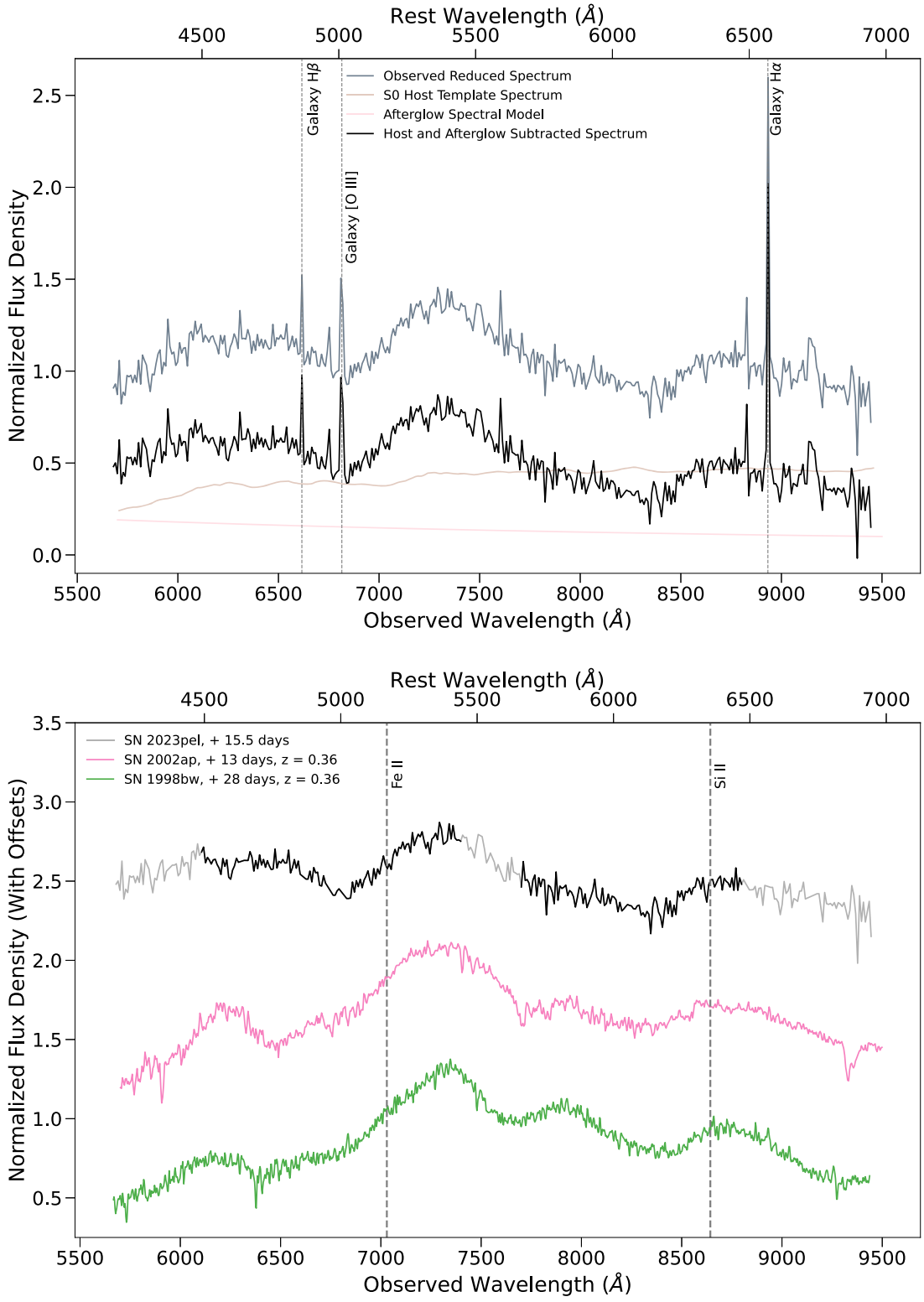

Figure 4. Top panel: DEIMOS spectrum obtained of GRB 230812B/SN 2023pel, 15.5 days after the observed peak in the r band. We show the original reduced spectrum, the best-fit S0 host galaxy template spectrum from NGSF with its flux scaled to the time of the spectrum, the afterglow spectral model with its flux scaled to the time of the spectrum assuming $F_\nu \propto \nu^{-\beta_O}$ (where $\beta_O = 0.74$ is the optical spectral index), and the final host- and afterglow-subtracted spectrum of SN 2023pel, smoothed and normalized for display purposes. The spectrum shows the strong Hβ, Hα, and [O III] galaxy emission lines at $z = 0.36$. Bottom panel: we show the spectrum of SN 2023pel after manually removing narrow galaxy emission lines. We also show the observed spectrum of SN 2002ap, 13 days after peak and redshifted to $z = 0.36$, and of SN 1998bw, 28 days after peak and also redshifted to $z = 0.36$. All three spectra show broad Fe II and Si II features, characteristic of Type Ic-BL SNe, and we label the lines as well as show the broadened features in bold for SN 2023pel.

The full derivation of the model can be found in Cano et al. (2016), and here we provide a brief description of the components. The afterglow is modeled by two components—an impulsive energy input term and a continuous energy input term. The impulsive energy input term (Zhang & Mészáros 2001) is represented by a simple power law (Rowlinson et al.

2013),

$$L_{\rm SPL}(t) = \Lambda t^{-\alpha}, \tag{2}$$

where Λ is a normalization constant and α is the power-law decay index. We assume that $\alpha = \Gamma_\gamma + 1$, where Γ_γ is the photon index of the prompt emission. This definition of α comes from the assumption that the decay slope is governed by the curvature effect (Panaitescu & Kumar 2000; Piran 2004).

The continuous energy input term is due to the magnetar central engine depositing Poynting flux into the ejecta, where the neutron star is assumed to have a mass of $1.4\,M_\odot$ and a radius of 10^6 cm. This emission creates a characteristic plateau in the LC and is represented as

$$L_{\rm AG}(t) = L_0\left(1 + \frac{t}{t_0}\right)^{-2}, \tag{3}$$

where L_0 is the luminosity of the plateau emission and t_0 is the duration of the plateau.

Finally, the SN component is modeled by the central engine depositing its energy directly into the SN after the initial jet spreads. The analytical prescription has been derived in many works (Ostriker & Gunn 1971; Kasen & Bildsten 2010; Barkov & Komissarov 2011; Chatzopoulos et al. 2011), and the equation (Arnett 1980, 1982; Valenti et al. 2008; Chatzopoulos et al. 2009, 2011) is represented as

$$L_{\rm SN}(t) = \frac{E_{\rm p}}{t_{\rm p}} \exp\left(\frac{-x^2}{2}\right) \int_0^x \frac{z \exp\left(\frac{z^2}{2}\right)}{(1+yz)^2}\,{\rm d}z, \tag{4}$$

where $E_{\rm p}$ is the initial energy of the magnetar in units of erg, $t_{\rm p}$ is the characteristic spin-down time of the magnetar in units of days, $x = t/t_{\rm diff}$, $y = t_{\rm diff}/t_{\rm p}$, and $t_{\rm diff}$ is the diffusion timescale of the SN in units of days. As mentioned earlier, all of this is considering an $l = 2$ dipole. We can rewrite $E_{\rm p}$ and $t_{\rm p}$ in terms of L_0 and t_0 through

$$E_{\rm p} = \frac{2.00}{2.05} L_0 t_0 \tag{5}$$

and

$$t_{\rm p} = 2\,t_0. \tag{6}$$

The final model we fit for the X-ray LC is

$$L^{\rm X-ray}_{\rm total}(t) = L_{\rm AG} + L_{\rm SPL}, \tag{7}$$

and the optical LC, which we fit to the r band, is

$$L^{r}_{\rm total}(t) = L_{\rm AG} + \Phi L_{\rm SN} + L_{\rm SPL}, \tag{8}$$

where Φ is an additional free parameter used to normalize the model to the optical data. Even if the properties of the magnetar derived from the X-ray and optical LCs match, if $\Phi > 1$, an additional source of energy is necessary to power the SN in addition to the magnetar central engine.

Finally, after fitting the observed LCs with the models presented, the derived L_0 and t_0 can be used to find B_0 and P_0 through

$$\frac{B_0}{10^{15}\,{\rm G}} = \sqrt{\frac{4.2}{L_{0,49} t_{0,3}^2}} \tag{9}$$

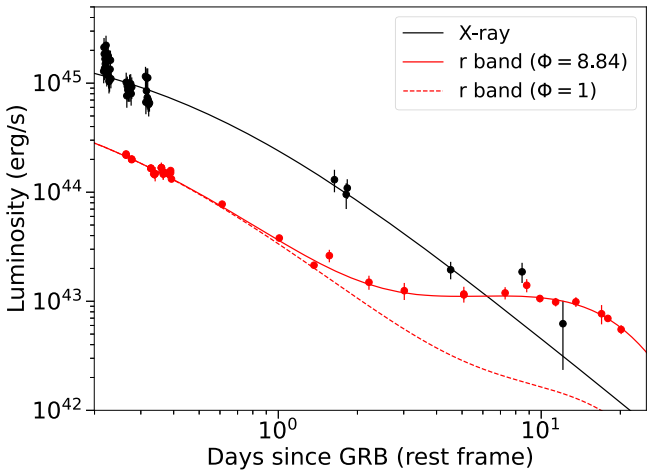

Figure 5. The magnetar model from Cano et al. (2016) fit to both the Swift XRT X-ray LC and the r-band LC of GRB 230812B/SN 2023pel independently. The derived properties of the magnetar are not consistent when comparing the X-ray and optical analysis, where we find that $B_0 = 3.37^{+0.91}_{-0.63} \times 10^{15}$ G and $P_0 = 14.44^{+2.29}_{-1.93}$ ms from the X-ray fitting and $B_0 = 1.07^{+0.13}_{-0.12} \times 10^{16}$ G and $P_0 = 32.41^{+2.67}_{-2.48}$ ms from the optical fitting. We find that an additional flux-stretching factor of $\Phi = 8.84^{+0.62}_{-0.63}$ is necessary to fit for the SN bump in the r-band LC, and we show the r-band LC with and without the inclusion of this stretching factor in the plot. These findings all show that the magnetar model is not viable to describe the LC of GRB 230812B/SN 2023pel, and that an additional source of power is necessary to describe the observed flux.

and

$$\frac{P_0}{1\ {\rm ms}} = \sqrt{\frac{2.05}{L_{0,49} t_{0,3}}}, \tag{10}$$

where $L_{0,49} = L_0/10^{49}$ erg s^{-1} and $t_{0,3} = t_0/10^3$ s.

Given this formulation, we begin by fitting Equation (7) to the Swift XRT LC, where we convert the 0.3–10 keV flux LC to a rest-frame 0.310 keV X-ray luminosity LC through the same method described in Section 3 of Cano et al. (2016), fitting the power-law decay index to $\alpha = \Gamma_\gamma + 1 = 3.16$ (Scotton et al. 2023). The best-fit LC is shown in black in Figure 5, and we derive $L_0 = 2.62^{+0.45}_{-0.28} \times 10^{45}$ erg s^{-1} and $t_0 = 3.75^{+0.51}_{-0.61} \times 10^4$ s. This in turn corresponds to $B_0 = 3.37^{+0.91}_{-0.63} \times 10^{15}$ G and $P_0 = 14.44^{+2.29}_{-1.93}$ ms. We then convert our r-band LC into luminosity space and fit Equation (8) to the LC, where the best-fit LC is shown in red in Figure 5. We derive $L_0 = 1.03 \pm 0.09 \times 10^{45}$ erg s^{-1}, $t_0 = 1.89^{+0.15}_{-0.13} \times 10^4$ s, and $\Phi = 8.84^{+0.62}_{-0.63}$, which clearly shows that an additional source of energy is needed to power the SN. These parameters correspond to $B_0 = 1.07^{+0.13}_{-0.12} \times 10^{16}$ G and $P_0 = 32.41^{+2.67}_{-2.48}$ ms.

There is therefore a clear discrepancy found in the values derived for the magnetar through independently fitting the X-ray and optical LCs. This shows that the magnetar model under the assumption of a dipolar, unevolving magnetic field is not viable to satisfactorily describe the observed phases of GRB 230812B/SN 2023pel.

4.2. Arnett Model and SN Parameters

We then consider the conventional Arnett (1982) model. This model, also known as the radioactive heating model, assumes that the optical emission is due to the decay of ^{56}Ni to ^{56}Co and to ^{56}Fe. We use Equation (36) from Arnett (1982) to

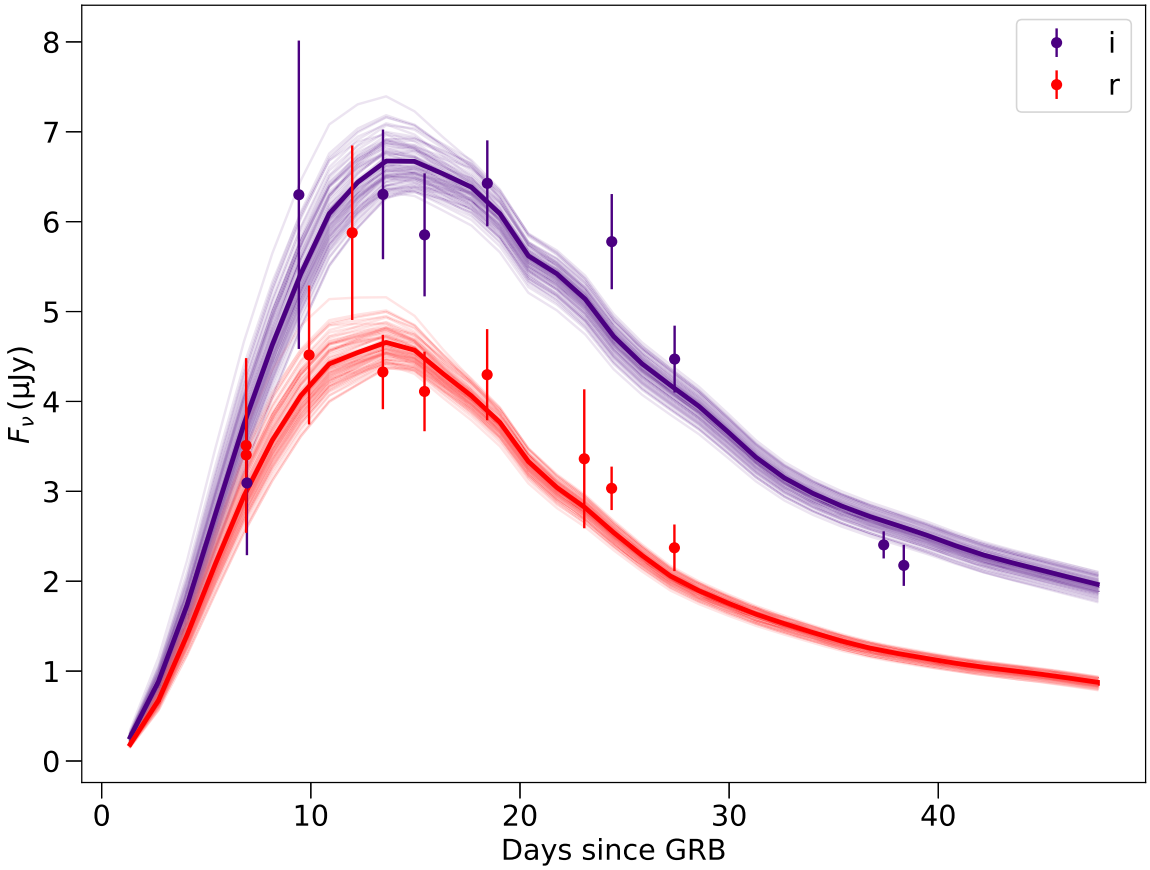

Figure 6. The afterglow and host-subtracted SN flux LC of SN 2023pel, corrected for Galactic extinction. In addition, we plot the best-fit *r*- and *i*-band flux LCs in the observer frame obtained from the best-fit bolometric LC constructed from the A82 radioactive heating SN model, assuming that the color and spectral evolution of SN 2023pel is identical to that of SN 2002ap. We derive the best-fit values $M_{\rm Ni} = 0.38 \pm 0.01\ M_\odot$ and $\tau_{\rm m} = 7.64^{+0.34}_{-0.33}$ days. One hundred possible random a posteriori models from the MCMC fitting samples are also plotted, with the best fits shown in bold.

model the bolometric optical luminosity, assuming full gamma-ray trapping of the ejecta, in addition to further radioactive inputs (Valenti et al. 2008). The ^{56}Ni mass is a key parameter that can be used to provide insights into both the explosion and the progenitor and is one of the major SN parameters we fit for in our modeling.

In order to fit the Arnett (1982) model, we begin by isolating the SN flux by subtracting the best-fit power law from Section 3.1 from the observed photometry after $T_0 + 5$ days, when the afterglow has faded enough for the SN flux to make relevant contributions to the LC. SN 2023pel's flux LC, corrected for Galactic extinction, is shown in Figure 6. We then generate semianalytic bolometric luminosity LC models from Arnett (1982) using the Hybrid Analytic Flux FittEr for Transients (Yang & Sollerman 2023), where the two free parameters are the nickel mass ($M_{\rm Ni}$) and the photon diffusion timescale ($\tau_{\rm m}$). $\tau_{\rm m}$ is an important parameter that relates to the mass of the total ejecta and the kinetic energy of the explosion, which we will show in Section 3.3.

Given a bolometric luminosity LC from the models, we need to extract associated *r*- and *i*-band LCs corresponding to the models to compare to our observed photometry. We do so through a similar method as in Srinivasaragavan et al. (2023), where we use bolometric correction (BC) coefficients at every epoch to convert from a bolometric luminosity LC to individual filter LCs, assuming that the color and spectral evolution of the SN is identical to that of the Type Ic-BL SN 2002ap (see Section 3.3; Mazzali et al. 2002). The BCs are defined as

$$\mathrm{BC}_x = M_{\rm bol} - M_x, \tag{11}$$

where x is the relevant filter, $M_{\rm bol}$ is the optical absolute bolometric magnitude, and M_x is the absolute magnitude in the relevant filter. For stripped-envelope SNe in the photospheric phase, the *g*-band coefficient (Lyman et al. 2014) is

$$\mathrm{BC}_g = 0.054\text{–}0.195 \times (g - r) - 0.719 \times (g - r)^2. \tag{12}$$

We derive the *g*-band coefficients at every epoch from an SN 2002ap–like LC at $z = 0.36$ generated through SNCOSMO, as well as the $g - r$ and $g - i$ colors. Then, at every epoch, we convert the bolometric luminosity computed from the Arnett (1982) model to a bolometric absolute magnitude and use Equation (11) to compute a *g*-band LC. Finally, we use the associated $g - r$ and $g - i$ colors at every epoch to generate *r*- and *i*-band LCs. After applying the correct distance modulus and *k*-corrections to these LCs, we compare them to our observed SN flux using Markov Chain Monte Carlo (MCMC) techniques with the `Python` package EMCEE (Foreman-Mackey et al. 2013) to fit for the nickel mass and the photon diffusion timescale, which have uniform priors corresponding to values derived in the literature (Corsi et al. 2016; Taddia et al. 2019; Corsi et al. 2023). We note that this method (though using an SN 1998bw–like LC instead) was also used to estimate the nickel mass of SN 2022xiw, the SN associated with GRB 221009A, in Srinivasaragavan et al. (2023). They derived results consistent with those of Blanchard et al. (2023),

who analyzed a JWST NIRSpec spectrum to constrain the nickel mass of SN 2022xiw.

The best-fit LCs from our fitting are shown in Figure 6. We derive $M_{\rm Ni} = 0.38 \pm 0.01\,M_{\odot}$ and $\tau_{\rm m} = 7.64^{+0.34}_{-0.33}$. We note that this error is the statistical uncertainty, and there are likely systematic uncertainties that arise from the Arnett (1982) model. Specifically, the assumptions of spherical symmetry along with full gamma-ray trapping of the ejecta play the biggest role in these uncertainties. The $M_{\rm Ni}$ we find is consistent with studies of SN 1998bw ($M_{\rm Ni} = 0.3$–$0.9\,M_{\odot}$; Sollerman et al. 2000). This is expected, as the brightness of the SN is about the same as SN 1998bw (see Section 3.2), and the nickel mass is a proxy for the brightness of the SN. These values correspond to a peak bolometric luminosity of $L_{\rm bol} \sim 1.3 \times 10^{43}\,{\rm erg\,s^{-1}}$, which is consistent with the average found for the overall GRB-SN sample of $L_{\rm bol} = 1 \times 10^{43}\,{\rm erg\,s^{-1}}$ with dispersion $\sigma = 0.4 \times 10^{43}\,{\rm erg\,s^{-1}}$ (Cano et al. 2017a).

We then estimate the photospheric expansion velocity ($v_{\rm ph}$) through measuring the absorption velocity of the Fe II feature at 5169 Å from the SN spectrum (shown in Figure 4), which has been shown to be a good proxy for $v_{\rm ph}$ (Modjaz et al. 2016). We use the same method as Anand et al. (2023), using `SESNSpectraPCA` (Williamson et al. 2019) to smooth the spectrum. We then use `SESNSpectraLib` (Liu et al. 2016; Modjaz et al. 2016) to fit for the Fe II absorption velocity by convolving the spectrum with Type Ic SN templates. From our fitting procedure, we estimate that $v_{\rm ph} = 11{,}300 \pm 1600\,{\rm km\,s^{-1}}$. This is lower than the velocities expected at peak for Type Ic-BL SNe but consistent with values derived for spectra taken around the same phase after peak for other Type Ic-BL events (Modjaz et al. 2016; Taddia et al. 2019). For a sanity check, we estimate the photospheric velocity for SN 2002ap (Mazzali et al. 2002) and SN 1998bw (Patat et al. 2001) at the phases of the best-fit SNID templates. We find that $v_{\rm ph} = 11{,}900 \pm 1150\,{\rm km\,s^{-1}}$ for SN 2002ap and $v_{\rm ph} = 14{,}100 \pm 800\,{\rm km\,s^{-1}}$ for SN 1998bw. Therefore, the photospheric velocities we estimate for SN 2023pel are consistent with SN 2002ap at the 1σ level at a similar phase and with SN 1998bw at the 2σ level at a later phase corresponding to a best-fit template from SNID.

Given τ_m and $v_{\rm ph}$, we can derive the total mass ejected in SN 2023pel ($M_{\rm ej}$) and the total kinetic energy of the explosion ($E_{\rm KE}$) using the equations from Lyman et al. (2016). Assuming that the explosion is a constant density sphere undergoing homologous expansion, $M_{\rm ej}$ is described as

$$M_{\rm ej} = \frac{\tau_{\rm m}^2 \beta c v_{\rm sc}}{2\kappa_{\rm opt}}, \tag{13}$$

and $E_{\rm KE}$ is described as

$$E_{\rm KE} = \frac{3 v_{\rm sc}^2 M_{\rm ej}}{10}, \tag{14}$$

where $\beta = 13.8$ is a constant, c is the speed of light, $\kappa_{\rm opt}$ is a constant average optical opacity, and $v_{\rm sc}$ is observationally set to the photospheric velocity $v_{\rm ph}$ at maximum light. We note that the $\kappa_{\rm opt}$ for stripped-envelope SNe varies in the literature (Nagy 2018 quotes $\kappa_{\rm opt} = 0.18\,{\rm cm^{-2}\,g^{-1}}$ for Type Ib SNe and $\kappa_{\rm opt} = 0.10\,{\rm cm^{-2}\,g^{-1}}$ for Type Ic SNe), but we adopt the value used by Chugai (2000), Tartaglia et al. (2021), and Barbarino et al. (2020) for stripped-envelope SNe, $\kappa_{\rm opt} = 0.7\,{\rm cm^{-2}\,g^{-1}}$, shown to accurately model observed stripped-envelope SNe in hydrodynamical LCs (Taddia et al. 2018). Because our observed spectrum is taken 15.5 days after the peak, we cannot use the photospheric velocity we derived earlier to estimate these parameters and can only derive lower limits. We find $M_{\rm ej} > 0.58\,M_{\odot}$ and $E_{\rm KE} > 3.2 \times 10^{50}$ erg.

In order to derive $v_{\rm sc}$ and these parameters, we use the photospheric velocity evolution of the Type Ic-BL SN sample from Modjaz et al. (2016) to estimate SN 2023pel's photospheric velocity at maximum light. Using the values from Table 3 in Modjaz et al. (2016), we find the median photospheric velocities and standard deviations at every time epoch between −15 and 20 days from maximum light and shift the median and 1σ time evolution curves to our derived velocity, $v_{\rm ph} = 11{,}300 \pm 1600\,{\rm km\,s^{-1}}$, at 11.3 rest-frame days after SN 2023pel's observed peak. We then extrapolate to the time of maximum light (0 days) and derive $v_{\rm sc} = 14{,}800 \pm 7500\,{\rm km\,s^{-1}}$, which is broadly consistent with the results from Hussenot-Desenonges et al. (2023), who derive a photospheric velocity at peak of $v_{\rm sc} = 17{,}114 \pm 2993\,{\rm km\,s^{-1}}$. Then, using the derived photospheric velocity at peak, we find $M_{\rm ej} = 1.0 \pm 0.6\,M_{\odot}$ and $E_{\rm KE} = 1.3^{+3.3}_{-1.2} \times 10^{51}$ erg.

4.3. Comparison to GRB-SN Population

Here, we contextualize GRB 230812B/SN 2023pel with respect to the overall GRB-SN population. The average values and dispersion of $k_{\rm SN1998bw}$ and $M_{\rm Ni}$ for the GRB-SN population are $k_{\rm SN1998bw} = 0.95$ with $\sigma = 0.45$ and $M_{\rm Ni} = 0.37\,M_{\odot}$ with $\sigma = 0.20\,M_{\odot}$ (Cano et al. 2017a). Therefore, the $k_{\rm SN1998bw}$ and $M_{\rm Ni}$ we derive for SN 2023pel are consistent with the overall GRB-SN population. The average values and dispersion of $M_{\rm ej}$ and $E_{\rm KE}$ for previous GRB-SN are $M_{\rm ej} = 6\,M_{\odot}$ with a dispersion $\sigma = 4\,M_{\odot}$ and $E_{\rm KE} = 2.5 \times 10^{52}$ erg with a dispersion $\sigma = 1.8 \times 10^{52}$ erg (Cano et al. 2017a). We find that our derived ejecta masses and kinetic energies are slightly lower than those of the overall population. This is due to the quick time evolution of the SN, leading to a relatively low photon diffusion timescale.

Because most luminous LGRBs are cosmological in origin, their associated SNe are too faint for current optical facilities to detect. However, GRB 221009A provided a rare example of an extremely energetic ($E_{\gamma,\rm iso} = 1 \times 10^{55}$ erg; Burns et al. 2023) and luminous ($L_{\gamma,\rm iso} = 2.1 \times 10^{54}\,{\rm erg\,s^{-1}}$; Frederiks et al. 2023b) LGRB that was close enough ($z = 0.151$) to study its associated SN. Despite GRB 221009A's large gamma-ray energy, its associated SN's properties were consistent with the overall GRB-SN population (Levan et al. 2023b; Blanchard et al. 2023; Fulton et al. 2023; Kann et al. 2023; Shrestha et al. 2023; Srinivasaragavan et al. 2023), and its brightness may have in fact been a little lower than the average seen in the population. The prompt emission from GRB 230812B is not nearly as energetic or luminous as GRB 221009A, but its properties are still on the high end with respect to the GRB-SN population. Therefore, it provides us with another opportunity to understand where SN parameters lie in the higher-energy regime of the GRB-SN population.

In Figure 7, we add GRB 230812B/SN 2023pel to a modification of Figure 5 from Srinivasaragavan et al. (2023) and compare the GRBs' $E_{\gamma,\rm iso}$ to their associated SN's $k_{\rm SN\ 1998bw}$ and $M_{\rm Ni}$, classifying the GRBs into low-luminosity ($L_{\gamma,\rm iso} < 10^{48.5}\,{\rm erg\,s^{-1}}$) and high-energy jet ($L_{\gamma,\rm iso} > 10^{49.5}\,{\rm erg\,s^{-1}}$) GRBs, with events in between labeled as intermediate GRBs. We shift our focus from the average isotropic gamma-ray luminosities for GRBs analyzed in

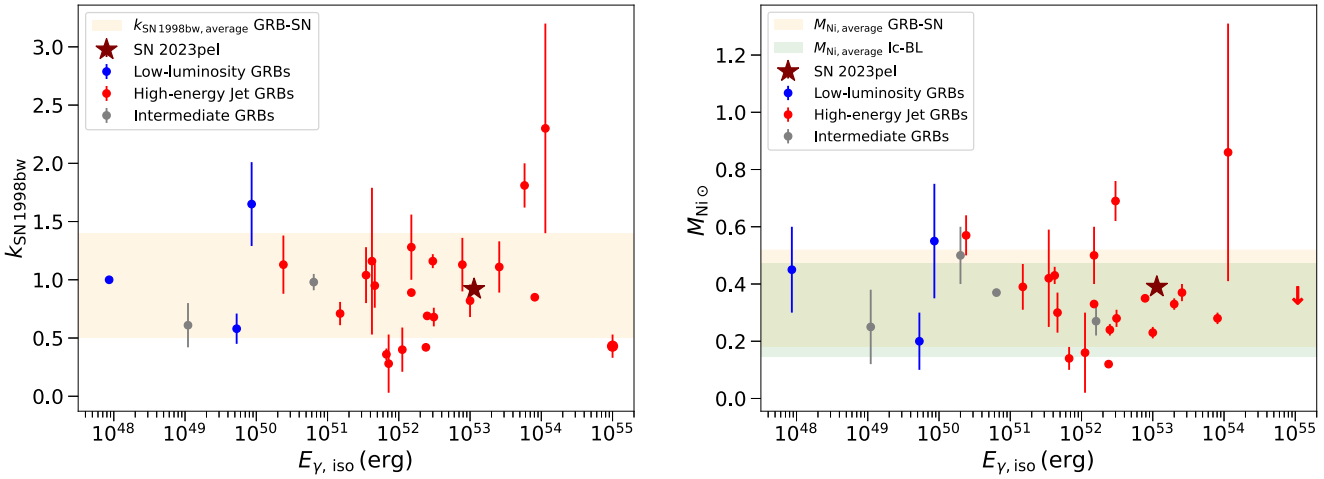

Figure 7. Left panel: modification of Figure 5 from Srinivasaragavan et al. (2023), where $k_{SN1998bw}$ is plotted against the isotropic equivalent gamma-ray energy ($E_{\gamma,iso}$) for observationally confirmed GRB-SNe. The plot distinguishes between low-luminosity GRBs, high-energy jet GRBs, and GRBs in the intermediate regime and also shows the average $k_{SN1998bw}$ for GRB-SNe in the plot and its dispersion without accounting for GRB 230812B/SN 2023pel. We indicate the results from this work, GRB 230812B/SN 2023pel, with a maroon star. Right panel: a similar update of Figure 5 from Srinivasaragavan et al. (2023), where the M_{Ni} in $M_{\odot}$ of GRB-SNe is plotted against the isotropic equivalent gamma-ray energy ($E_{\gamma,iso}$) from the prompt emission for the GRBs. The same distinctions for GRBs are made as for the left panel, and we show the results from this work with a maroon star. We also show the average M_{Ni}, along with its dispersion, for GRB-SNe in the plot, with the exception of GRB 230812B/SN 2023pel, as well as GRB 221009A/SN 2022xiw, because only a robust upper limit was derived for the event from Srinivasaragavan et al. (2023). We also show the average M_{Ni}, along with its dispersion, for the Type Ic-BL SN sample not associated with GRBs from Taddia et al. (2019).

Srinivasaragavan et al. (2023) to their isotropic equivalent gamma-ray energies instead, as it is a more relevant property for comparisons between the associated SN's parameters connected to its luminosity ($k_{SN\,1998bw}$ and M_{Ni}). We also plot the average $k_{SN1998bw}$ for the GRB-SN population and M_{Ni} for the GRB-SN and overall Type Ic-BL SN population (Taddia et al. 2019) in the figure. We find that SN 2023pel's properties are very ordinary with respect to the rest of the GRB-SN population.

Srinivasaragavan et al. (2023) also tested for statistical correlations between $L_{\gamma,iso}$ and $k_{SN\,1998bw}$ and between $L_{\gamma,iso}$ and M_{Ni}, and they found no significant correlations present. We do the same with $E_{\gamma,iso}$ for the high-energy jet GRB population and the entire population using the Pearson correlation coefficient test. For the nickel mass, we find a coefficient of 0.40 and a p-value of 0.18 for the high-energy jet GRBs and a coefficient of 0.35 with a p-value of 0.19 for the entire population. For $k_{SN\,1998bw}$, we find a coefficient of -0.16 and a p-value of 0.48 for the high-energy jet GRBs and a coefficient of -0.15 with a p-value of 0.46 for the entire population. Therefore, there are again no significant correlations present. This, along with other events in the literature (see, e.g., Tanvir et al. 2010; MichałowskI et al. 2018), suggests a decoupling between the central engine activity that powers relativistic ejecta in GRBs and SN emission in GRB-SN systems.

5. Conclusion

We analyze the optical counterpart of GRB 230812B and determine that it possesses a late-time flattening consistent with an associated SN, SN 2023pel. SN 2023pel has a peak r-band magnitude of $M_r = -19.46 \pm 0.18$ mag and a similar brightness to SN 1998bw while evolving on quicker timescales. We confirm that SN 2023pel is a Type Ic-BL SN through analyzing a spectrum taken by DEIMOS 15.5 days after the SN peak in the r band and confirming broad Fe II and Si II features. We then rule out a millisecond magnetar central engine powering the GRB-SN (Cano et al. 2016) in the context of a dipolar, unevolving magnetic field through an independent fitting of the X-ray and optical LCs. Using the Arnett (1982) radioactive decay model, we find that SN 2023pel has a nickel mass $M_{Ni} = 0.38 \pm 0.01\,M_{\odot}$, which is consistent with both the GRB-SN population and the overall Type Ic-BL SN population. We derive a photospheric expansion velocity of $v_{ph} = 11{,}300 \pm 1600$ km s^{-1} at that phase and extrapolate a velocity at maximum light of $v_{ph} = 14{,}800 \pm 7500$ km s^{-1}. Using this velocity, we derive estimates of the ejecta mass and kinetic energy: $M_{ej} = 1.0 \pm 0.6\,M_{\odot}$ and $E_{KE} = 1.3^{+3.3}_{-1.2} \times 10^{51}$ erg.

Our analysis of GRB 230812B/SN 2023pel shows that SN 2023pel is a rather ordinary SN with respect to the overall GRB-SN population. GRB 230812B/SN 2023pel adds more evidence that the central engine and SN-powering mechanisms are decoupled in GRB-SN systems. As optical surveys become more sensitive in the future, we will uncover more GRB-SN events that possess an $E_{\gamma,iso}$ between those of GRB 230812B and GRB 221009A, a region of the parameter space that has been sparsely explored, as seen in Figure 7. These events have the potential to help understand why this decoupling between the GRB central engine and SN emission occurs. Therefore, we encourage future studies of nearby energetic GRB-SNe in order to continue shedding light on the outstanding open questions of the GRB-SN connection.

Acknowledgments

G.P.S. dedicates this paper to Keagan Jaravata and to the Alvir and Jaravata families. SN 2023pel will always be connected to the memory of Keagan's life.

G.P.S. thanks Isiah Holt for useful discussions on MCMC techniques and Simi Bhullar for her moral support throughout the paper-writing process. The material is based upon work supported by NASA under award No. 80GSFC21M0002. B.O. acknowledges useful discussions with Noel Klingler regarding UVOT data analysis and the impact of the ongoing attitude control issues. B.O. gratefully acknowledges support from the McWilliams Postdoctoral Fellowship at Carnegie Mellon University. M.C.M. was supported in part by NASA ADAP grants 80NSSC21K0649 and 80NSSC20K0288. G.C.A. thanks

the Indian National Science Academy for support under the INSA Senior Scientist program. M.W.C. acknowledges support from the National Science Foundation with grant No. PHY-2010970 and OAC-2117997. S.Y. is supported by the National Natural Science Foundation of China under grant No. 12303046.

These results made use of Lowell Observatory's Lowell Discovery Telescope (LDT), formerly the Discovery Channel Telescope. Lowell operates the LDT in partnership with Boston University, Northern Arizona University, the University of Maryland, and the University of Toledo. Partial support of the LDT was provided by Discovery Communications. LMI was built by Lowell Observatory using funds from the National Science Foundation (AST-1005313). The GROWTH-India Telescope (GIT) is a 70 cm telescope with a $0\overset{\circ}{.}7$ field of view set up by the Indian Institute of Astrophysics (IIA) and the Indian Institute of Technology Bombay (IITB) with funding from the Indo-US Science and Technology Forum and the Science and Engineering Research Board, Department of Science and Technology (DST), Government of India. It is located at the Indian Astronomical Observatory (Hanle), operated by IIA, an autonomous institute under DST. We acknowledge funding by the IITB alumni batch of 1994, which partially supports operations of the telescope. Telescope technical details are available at https://sites.google.com/view/growthindia/. The 2 m Himalayan Chandra Telescope (HCT) is located at the Indian Optical Observatory (IAO) at Hanle. We thank the staff of IAO, Hanle, and CREST, Hosakote, that made these observations possible. HCT observations were carried out under the ToO program of proposal No. HCT-2023-C2-P15. The facilities at IAO and CREST are operated by the Indian Institute of Astrophysics, Bangalore. The Liverpool Telescope is operated on the island of La Palma by Liverpool John Moores University in the Spanish Observatorio del Roque de los Muchachos of the Instituto de Astrofisica de Canarias with financial support from the UK Science and Technology Facilities Council.

Some of the data presented herein were obtained at the W. M. Keck Observatory, which is operated as a scientific partnership among the California Institute of Technology, the University of California, and the National Aeronautics and Space Administration. The Observatory was made possible by the generous financial support of the W. M. Keck Foundation. The authors wish to recognize and acknowledge the very significant cultural role and reverence that the summit of Maunakea has always had within the indigenous Hawaiian community. We are most fortunate to have the opportunity to conduct observations from this mountain. SED Machine is based upon work supported by the National Science Foundation under grant No. 1106171. Based on observations obtained with the Samuel Oschin Telescope 48 inch and the 60 inch telescope at the Palomar Observatory as part of the Zwicky Transient Facility project. ZTF is supported by the National Science Foundation under grant No. AST-2034437 and a collaboration including Caltech, IPAC, the Weizmann Institute of Science, the Oskar Klein Center at Stockholm University, the University of Maryland, Deutsches Elektronen-Synchrotron and Humboldt University, the TANGO Consortium of Taiwan, the University of Wisconsin at Milwaukee, Trinity College Dublin, Lawrence Livermore National Laboratories, IN2P3, the University of Warwick, Ruhr University Bochum, and Northwestern University. Operations are conducted by COO, IPAC, and UW. The ZTF forced-photometry service was funded under Heising–Simons Foundation grant No. 12540303 (PI: Graham). The Gordon and Betty Moore Foundation, through both the Data-Driven Investigator Program and a dedicated grant, provided critical funding for SkyPortal.

Facilities: PO:1.2m, PO:1.5m, Liverpool:2m, LDT, HCT, Keck:II.

Software: PYMULTINEST, WOMBAT, SESNSPECTRAPCA, SESNSPECTRALIB, PYPEIT, SNCOSMO, PYSPECKIT, XSPEC V12.12.0, EMCEE, SCAMP, SWARP, ZOGY, SEXTRACTOR, ASTRO-SCRAPPY, SOLVE-FIELD, HEASOFT V6.29C, FPIPE.

Appendix

In Table 1 we show the optical photometry obtained of GRB 230812B/SN 2023pel.

Table 1
Optical Photometry and 1σ Errors of GRB 230812B/SN 2023pel

$t_{obs} - T_0$ (days)	Telescope	Filter	AB mag	Uncertainty
0.359	ZTF	*r*	18.85	0.04
0.359	ZTF	*r*	18.85	0.04
0.359	ZTF	*r*	18.83	0.02
0.377	ZTF	*r*	18.95	0.03
0.377	ZTF	*r*	18.95	0.03
0.377	ZTF	*r*	18.96	0.01
0.393	ZTF	*g*	19.19	0.03
0.393	ZTF	*g*	19.19	0.03
0.393	ZTF	*g*	19.21	0.01
0.411	ZTF	*g*	19.22	0.03
0.411	ZTF	*g*	19.22	0.03
0.411	ZTF	*g*	19.29	0.03
0.446	ZTF	*r*	19.16	0.04
0.446	ZTF	*r*	19.16	0.04
0.446	ZTF	*r*	19.16	0.02
0.451	SEDM	*u*	19.84	0.2
0.455	SEDM	*g*	19.52	0.13
0.455	SEDM	*g*	19.52	0.13
0.457	SEDM	*r*	19.28	0.04
0.46	ZTF	*r*	19.3	0.09
0.46	SEDM	*i*	19.1	0.05
0.463	SEDM	*r*	19.28	0.16
0.489	ZTF	*r*	19.14	0.12
0.489	ZTF	*r*	19.14	0.12
0.489	ZTF	*r*	19.15	0.06
0.49	SEDM	*u*	19.69	0.23
0.494	SEDM	*g*	19.68	0.14
0.497	SEDM	*r*	19.29	0.04
0.497	ZTF	*r*	19.24	0.16
0.497	ZTF	*r*	19.24	0.16
0.497	ZTF	*r*	19.27	0.07
0.5	SEDM	*i*	19.15	0.05
0.518	ZTF	*r*	19.28	0.1
0.518	ZTF	*r*	19.28	0.1
0.518	ZTF	*r*	19.26	0.07
0.53	ZTF	*r*	19.26	0.12
0.53	ZTF	*r*	19.21	0.06
0.531	SEDM	*g*	19.89	0.13
0.534	SEDM	*r*	19.4	0.03
0.536	SEDM	*i*	19.32	0.04
0.832	GIT	*r*	19.98	0.05
0.85	GIT	*g*	20.34	0.06
0.868	GIT	*i*	19.71	0.06
1.368	SEDM	*g*	21.09	0.15

Table 1
(Continued)

$t_{obs} - T_0$ (days)	Telescope	Filter	AB mag	Uncertainty
1.372	SEDM	*r*	20.76	0.07
1.376	SEDM	*i*	20.79	0.12
1.86	GIT	*r*	21.38	0.05
2.125	LT	*g*	21.77	0.24
2.127	LT	*r*	21.16	0.14
2.129	LT	*i*	21.15	0.18
3.009	HCT	*r*	21.77	0.16
4.1	LT	*r*	21.96	0.19
4.103	LT	*i*	22.47	0.3
6.907	HCT	*r*	22.04	0.18
6.91	GIT	*r*	22.06	0.1
6.945	HCT	*i*	22.04	0.15
9.427	SEDM	*i*	21.67	0.23
9.916	HCT	*r*	22.02	0.14
11.979	HCT	*r*	21.84	0.15
13.445	LDT	*r*	22.14	0.08
13.45	LDT	*i*	21.76	0.11
15.436	LDT	*r*	22.22	0.1
15.439	LDT	*i*	21.86	0.11
18.43	LDT	*r*	22.22	0.11
18.438	LDT	*i*	21.8	0.07
23.074	LT	*r*	22.49	0.22
24.382	LDT	*r*	22.6	0.07
24.388	LDT	*i*	21.94	0.09
27.384	LDT	*r*	22.85	0.1
27.394	LDT	*i*	22.21	0.08
37.385	LDT	*r*	>24.29	⋯
37.390	LDT	*i*	22.86	0.06
38.340	LDT	*r*	>24.12	⋯
38.351	LDT	*i*	22.96	0.1

Note. The photometry includes contributions from the afterglow and associated SN and are all image-subtracted to correct for the host galaxy contribution. All times are in the observer frame, and the magnitudes are not corrected for Galactic extinction.

ORCID iDs

Gokul P. Srinivasaragavan https://orcid.org/0000-0002-6428-2700
Vishwajeet Swain https://orcid.org/0000-0002-7942-8477
Brendan O'Connor https://orcid.org/0000-0002-9700-0036
Shreya Anand https://orcid.org/0000-0003-3768-7515
Tomás Ahumada https://orcid.org/0000-0002-2184-6430
Daniel Perley https://orcid.org/0000-0001-8472-1996
Robert Stein https://orcid.org/0000-0003-2434-0387
Jesper Sollerman https://orcid.org/0000-0003-1546-6615
Christoffer Fremling https://orcid.org/0000-0002-4223-103X
S. Bradley Cenko https://orcid.org/0000-0003-1673-970X
S. Antier https://orcid.org/0000-0002-7686-3334
Nidhal Guessoum https://orcid.org/0000-0003-1585-8205
Thomas Hussenot-Desenonges https://orcid.org/0009-0009-2434-432X
Stephen Lesage https://orcid.org/0000-0001-8058-9684
Erica Hammerstein https://orcid.org/0000-0002-5698-8703
M. Coleman Miller https://orcid.org/0000-0002-2666-728X
Igor Andreoni https://orcid.org/0000-0002-8977-1498
Varun Bhalerao https://orcid.org/0000-0002-6112-7609
Joshua S. Bloom https://orcid.org/0000-0002-7777-216X
Anirban Dutta https://orcid.org/0000-0002-7708-3831
Avishay Gal-Yam https://orcid.org/0000-0002-3653-5598
K-Ryan Hinds https://orcid.org/0000-0002-0129-806X
Amruta Jaodand https://orcid.org/0000-0002-3850-6651
Mansi Kasliwal https://orcid.org/0000-0002-5619-4938
Harsh Kumar https://orcid.org/0000-0003-0871-4641
Alexander S. Kutyrev https://orcid.org/0000-0002-2715-8460
Fabio Ragosta https://orcid.org/0000-0003-2132-3610
Vikram Ravi https://orcid.org/0000-0002-7252-5485
Kritti Sharma https://orcid.org/0000-0002-4477-3625
Rishabh Singh Teja https://orcid.org/0000-0002-0525-0872
Sheng Yang https://orcid.org/0000-0002-2898-6532
G. C. Anupama https://orcid.org/0000-0003-3533-7183
Eric C. Bellm https://orcid.org/0000-0001-8018-5348
Michael W. Coughlin https://orcid.org/0000-0002-8262-2924
Frank J. Masci https://orcid.org/0000-0002-8532-9395
Utkarsh Pathak https://orcid.org/0009-0002-7897-6110
Josiah Purdum https://orcid.org/0000-0003-1227-3738
Oliver J. Roberts https://orcid.org/0000-0002-7150-9061
Roger Smith https://orcid.org/0000-0001-7062-9726
Avery Wold https://orcid.org/0000-0002-9998-6732

References

Abazajian, K. N., Adelman-McCarthy, J. K., Agüeros, M. A., et al. 2009, ApJS, 182, 543
Agui Fernandez, J. F., de Ugarte Postigo, A., Thoene, C. C., et al. 2023, GCN, 34597, 1
Ahumada, T., Anand, S., Coughlin, M. W., et al. 2022, ApJ, 932, 40
Ahumada, T., Singer, L. P., Anand, S., et al. 2021, NatAs, 5, 917
Almualla, M., Coughlin, M. W., Anand, S., et al. 2020, MNRAS, 495, 4366
Anand, S., Barnes, J., Yang, S., et al. 2023, arXiv:2302.09226
Arnett, W. D. 1980, ApJ, 237, 541
Arnett, W. D. 1982, ApJ, 253, 785
Barbarino, C., Sollerman, J., Taddia, F., et al. 2020, arXiv:2010.08392
Barbary, K., Barclay, T., Biswas, R., et al., 2016, SNCosmo: Python Library for Supernova Cosmology, Astrophysics Source Code Library, ascl:1611.017
Barkov, M. V., & Komissarov, S. S. 2011, MNRAS, 415, 944
Beardmore, A. P., Melandri, A., Sbarrato, T., et al. 2023, GCN, 34400, 1
Bellm, E. C., Kulkarni, S. R., Barlow, T., et al. 2019, PASP, 131, 068003
Berger, E., Fong, W., & Chornock, R. 2013, ApJL, 774, L23
Bertin, E. 2006, in ASP Conf. Ser. 351, Astronomical Data Analysis Software and Systems XV, ed. C. Gabriel et al. (San Francisco, CA: ASP), 112
Bertin, E., 2010 SWarp: Resampling and Co-adding FITS Images Together, Astrophysics Source Code Library, ascl:1010.068
Bertin, E., & Arnouts, S. 1996, A&AS, 117, 393
Blagorodnova, N., Neill, J. D., Walters, R., et al. 2018, PASP, 130, 035003
Blanchard, P. K., Villar, V. A., Chornock, R., et al. 2023, arXiv:2308.14197
Blondin, S., & Tonry, J. L. 2007, ApJ, 666, 1024
Buchner, J., Georgakakis, A., Nandra, K., et al. 2014, A&A, 564, A125
Burns, E., Svinkin, D., Fenimore, E., et al. 2023, ApJL, 946, L31
Burrows, D. N., Hill, J. E., Nousek, J. A., et al. 2005, SSRv, 120, 165
Cano, Z. 2014, ApJ, 794, 121
Cano, Z., Johansson Andreas, K. G., & Maeda, K. 2016, MNRAS, 457, 2761
Cano, Z., Izzo, L., de Ugarte Postigo, A., et al. 2017b, A&A, 605, A107
Cano, Z., Wang, S.-Q., Dai, Z.-G., & Wu, X.-F. 2017a, AdAst, 2017, 8929054
Cardelli, J. A., Clayton, G. C., & Mathis, J. S. 1989, ApJ, 345, 245
Cash, W. 1979, ApJ, 228, 939
Cenko, B. 2023, GCN, 34633, 1
Chambers, K. C., Magnier, E. A., Metcalfe, N., et al. 2016, arXiv:1612.05560
Chatzopoulos, E., Wheeler, J. C., & Vinko, J. 2009, ApJ, 704, 1251
Chatzopoulos, E., Wheeler, J. C., Vinko, J., et al. 2011, ApJ, 729, 143
Chugai, N. N. 2000, AstL, 26, 797
Clocchiatti, A., Suntzeff, N. B., Covarrubias, R., & Candia, P. 2011, AJ, 141, 163
Corsi, A., Gal-Yam, A., Kulkarni, S. R., et al. 2016, ApJ, 830, 42
Corsi, A., Ho, A. Y. Q., Cenko, S. B., et al. 2023, ApJ, 953, 179
Coughlin, M. W., Antier, S., Corre, D., et al. 2019, MNRAS, 489, 5775
Coughlin, M. W., Bloom, J. S., Nir, G., et al. 2023, ApJS, 267, 31
Coughlin, M. W., Tao, D., Chan, M. L., et al. 2018, MNRAS, 478, 692
Cutri, R. M., Wright, E. L., Conrow, T., et al. 2013, Explanatory Supplement to the AllWISE Data Release Products

Dalessi, S., Roberts, O. J., Meegan, C., & Fermi, G. B. M. 2023, GCN, 33411, 1
de Ugarte Postigo, A., Agui Fernandez, J. F., Thoene, C. C., & Izzo, L. 2023, GCN, 34409, 1
Dekany, R., Smith, R. M., Riddle, R., et al. 2020, PASP, 132, 038001
Della Valle, M., Chincarini, G., Panagia, N., et al. 2006, Natur, 444, 1050
Duev, D. A., Mahabal, A., Masci, F. J., et al. 2019, MNRAS, 489, 3582
Evans, P. A., Beardmore, A. P., Page, K. L., et al. 2009, MNRAS, 397, 1177
Faber, S. M., Phillips, A. C., Kibrick, R. I., et al. 2003, Proc. SPIE, 4841, 1657
Feroz, F., Hobson, M. P., & Bridges, M. 2009, MNRAS, 398, 1601
Flesch, E. W. 2019, arXiv:1912.05614
Flewelling, H. A., Magnier, E. A., Chambers, K. C., et al. 2020, ApJS, 251, 7
Foreman-Mackey, D., Hogg, D. W., Lang, D., & Goodman, J. 2013, PASP, 125, 306
Frederiks, D., Svinkin, D., Lysenko, A. L., et al. 2023a, ApJL, 949, L7
Frederiks, D., Svinkin, D., Lysenko, A. L., et al. 2023b, ApJL, 949, L7
Fremling, C., Sollerman, J., Taddia, F., et al. 2016, A&A, 593, A68
Fulton, M. D., Smartt, S. J., Rhodes, L., et al. 2023, ApJL, 946, L22
Fynbo, J. P. U., Watson, D., Thöne, C. C., et al. 2006, Natur, 444, 1047
Galama, T. J., Vreeswijk, P. M., van Paradijs, J., et al. 1998, Natur, 395, 670
Gal-Yam, A., Fox, D. B., Price, P. A., et al. 2006, Natur, 444, 1053
Gehrels, N., Chincarini, G., Giommi, P., et al. 2004, ApJ, 611, 1005
Gillanders, J. H., Troja, E., Fryer, C. L., et al. 2023, arXiv:2308.00633
Ginsburg, A., & Mirocha, J., 2011 PySpecKit: Python Spectroscopic Toolkit, Astrophysics Source Code Library, ascl:1109.001
Ginsburg, A., Sokolov, V., de Val-Borro, M., et al. 2022, AJ, 163, 291
Goldstein, A., Cleveland, W. H., & Kocevski, D. 2022, Fermi GBM Data Tools: v1.1.1, https://fermi.gsfc.nasa.gov/ssc/data/analysis/gbm
Goldwasser, S., Yaron, O., Sass, A., et al. 2022, TNSAN, 191, 1
Graham, M. J., Kulkarni, S. R., Bellm, E. C., et al. 2019, PASP, 131, 078001
Granot, J., & Sari, R. 2002, ApJ, 568, 820
Greiner, J., Krühler, T., McBreen, S., et al. 2009, ApJ, 693, 1912
Greiner, J., Mazzali, P. A., Kann, D. A., et al. 2015, Natur, 523, 189
Hjorth, J. 2013, RSPTA, 371, 20120275
Hu, Y. D., Castro-Tirado, A. J., Kumar, A., et al. 2021, A&A, 646, A50
Hussenot-Desenonges, T., Wouters, T., Guessom, N., et al. 2023, arXiv:2310.14310
Iwamoto, K., Mazzali, P. A., Nomoto, K., et al. 1998, Natur, 395, 672
Kann, D. A., Agayeva, S., Aivazyan, V., et al. 2023, ApJL, 948, L12
Kann, D. A., Masetti, N., & Klose, S. 2007, AJ, 133, 1187
Kann, D. A., Schady, P., Olivares, E. F., et al. 2019, A&A, 624, A143
Kasen, D., & Bildsten, L. 2010, ApJ, 717, 245
Kasliwal, M. M., Anand, S., Ahumada, T., et al. 2020, ApJ, 905, 145
Kumar, A., Pandey, S. B., Gupta, R., et al. 2022a, NewA, 97, 101889
Kumar, H., Bhalerao, V., Anupama, G. C., et al. 2022b, AJ, 164, 90
Kumar, H., Bhalerao, V., Anupama, G. C., et al. 2022c, MNRAS, 516, 4517
Lang, D., Hogg, D. W., Mierle, K., Blanton, M., & Roweis, S. 2010, AJ, 139, 1782
Laskar, T., Alexander, K. D., Margutti, R., et al. 2023, ApJL, 946, L23
Lesage, S., Burns, E., Dalessi, S., Roberts, O., & Fermi, G. B. M. 2023a, GCN, 34387, 1
Lesage, S., Veres, P., Briggs, M. S., et al. 2023b, ApJL, 952, L42
Leśniewska, A., Michałowski, M. J., Kamphuis, P., et al. 2022, ApJS, 259, 67
Levan, A., Gompertz, B. P., Salafia, O. S., et al. 2023a, arXiv:2307.02098
Levan, A., Nugent, P., Fruchter, A., et al. 2005, ApJ, 624, 880
Levan, A. J., Lamb, G. P., Schneider, B., et al. 2023b, ApJL, 946, L28
LHAASO Collaboration, Cao, Z., Aharonian, F., et al. 2023, Sci, 380, 1390
Lipunov, V., Kornilov, V., Gorbovskoy, E., et al. 2023a, GCN, 34389, 1
Lipunov, V., Svinkin, D., Kuznetsov, A., et al. 2023b, GCN, 34396, 1
Liu, Y.-Q., Modjaz, M., Bianco, F. B., & Graur, O. 2016, ApJ, 827, 90
Lü, H.-J., Lan, L., Zhang, B., et al. 2018, ApJ, 862, 130
Lyman, J. D., Bersier, D., & James, P. A. 2014, MNRAS, 437, 3848
Lyman, J. D., Bersier, D., James, P. A., et al. 2016, MNRAS, 457, 328
Malesani, D., Tagliaferri, G., Chincarini, G., et al. 2004, ApJL, 609, L5
Malesani, D. B., Levan, A. J., Izzo, L., et al. 2023, arXiv:2302.07891
Mangan, J., Dunwoody, R., Meegan, C., & Fermi, G. B. M. 2021, GCN, 31210, 1
Masci, F. J., Laher, R. R., Rusholme, B., et al. 2019, PASP, 131, 018003
Matheson, T., Garnavich, P. M., Stanek, K. Z., et al. 2003, ApJ, 599, 394
Mazzali, P. A., Deng, J., Maeda, K., et al. 2002, ApJL, 572, L61
Mazzali, P. A., Deng, J., Nomoto, K., et al. 2006, Natur, 442, 1018
McCully, C., & Tewes, M., 2019 Astro-SCRAPPY: Speedy Cosmic Ray Annihilation Package in Python, Astrophysics Source Code Library, ascl:1907.032
Meegan, C., Lichti, G., Bhat, P. N., et al. 2009, ApJ, 702, 791
Melandri, A., Malesani, D. B., Izzo, L., et al. 2019, MNRAS, 490, 5366
MichałowskI, M. J., Xu, D., Stevens, J., et al. 2018, A&A, 616, A169
Modjaz, M., Liu, Y. Q., Bianco, F. B., & Graur, O. 2016, ApJ, 832, 108
Nagy, A. P. 2018, ApJ, 862, 143
Nasa High Energy Astrophysics Science Archive Research Center (Heasarc), 2014 HEAsoft: Unified Release of FTOOLS and XANADU, Astrophysics Source Code Library, ascl:1408.004
Oates, S. R., Page, M. J., Schady, P., et al. 2009, MNRAS, 395, 490
O'Connor, B., Troja, E., Ryan, G., et al. 2023, SciA, 9, eadi1405
Ostriker, J. P., & Gunn, J. E. 1971, ApJL, 164, L95
Page, K. L. & Swift-XRT Team 2023, GCN, 34394, 1
Panaitescu, A., & Kumar, P. 2000, ApJ, 543, 66
Patat, F., Cappellaro, E., Danziger, J., et al. 2001, ApJ, 555, 900
Patterson, M. T., Bellm, E. C., Rusholme, B., et al. 2019, PASP, 131, 018001
Piran, T. 2004, RvMP, 76, 1143
Prochaska, J., Hennawi, J., Westfall, K., et al. 2020, JOSS, 5, 2308
Rastinejad, J. C., Gompertz, B. P., Levan, A. J., et al. 2022, Natur, 612, 223
Rigault, M., Neill, J. D., Blagorodnova, N., et al. 2019, A&A, 627, A115
Roberts, O. J., Meegan, C., Lesage, S., et al. 2023, GCN, 34391, 1
Roming, P. W. A., Kennedy, T. E., Mason, K. O., et al. 2005, SSRv, 120, 95
Rossi, A., Piranomonte, S., Savaglio, S., et al. 2014, A&A, 572, A47
Rossi, A., Rothberg, B., Palazzi, E., et al. 2022, ApJ, 932, 1
Rowlinson, A., O'Brien, P. T., Metzger, B. D., Tanvir, N. R., & Levan, A. J. 2013, MNRAS, 430, 1061
Salgundi, A., Swain, V., Kumar, H., et al. 2023, GCN, 34397, 1
Sari, R., Piran, T., & Narayan, R. 1998, ApJL, 497, L17
Schlafly, E. F., & Finkbeiner, D. P. 2011, ApJ, 737, 103
Schulze, S., Malesani, D., Cucchiara, A., et al. 2014, A&A, 566, A102
Scotton, L., Kocevski, D., Racusin, J., Omodei, N. & Fermi-LAT Collaboration 2023, GCN, 34392, 1
Shrestha, M., Sand, D. J., Alexander, K. D., et al. 2023, ApJL, 946, L25
Sollerman, J., Kozma, C., Fransson, C., et al. 2000, ApJL, 537, L127
Srinivasaragavan, G. P., O'Connor, B., Cenko, S. B., et al. 2023, ApJL, 949, L39
Starling, R. L. C., Wiersema, K., Levan, A. J., et al. 2011, MNRAS, 411, 2792
Steele, I. A., Smith, R. J., Rees, P. C., et al. 2004, Proc. SPIE, 5489, 679
Stern, D., Assef, R. J., Benford, D. J., et al. 2012, ApJ, 753, 30
Stritzinger, M. D., Hamuy, M., Suntzeff, N. B., et al. 2002, AAS Meeting Abstracts, 200, 95.03
Tachibana, Y., & Miller, A. A. 2018, PASP, 130, 128001
Taddia, F., Sollerman, J., Fremling, C., et al. 2019, A&A, 621, A71
Taddia, F., Stritzinger, M. D., Bersten, M., et al. 2018, A&A, 609, A136
Tanga, M., Krühler, T., Schady, P., et al. 2018, A&A, 615, A136
Tanvir, N. R., Rol, E., Levan, A. J., et al. 2010, ApJ, 725, 625
Tartaglia, L., Sollerman, J., Barbarino, C., et al. 2021, A&A, 650, A174
Toma, K., Ioka, K., Sakamoto, T., & Nakamura, T. 2007, ApJ, 659, 1420
Toy, V. L., Cenko, S. B., Silverman, J. M., et al. 2016, ApJ, 818, 79
Troja, E., Fryer, C. L., O'Connor, B., et al. 2022, Natur, 612, 228
Usov, V. V. 1992, Natur, 357, 472
Valenti, S., Benetti, S., Cappellaro, E., et al. 2008, MNRAS, 383, 1485
van der Walt, S., Crellin-Quick, A., & Bloom, J. 2019, JOSS, 4, 1247
van der Walt, S. J., Crellin-Quick, A., & Bloom, J. S. 2019, JOSS, 4, 1247
Wang, J., Zhu, Z. P., Xu, D., et al. 2018, ApJ, 867, 147
Williams, M. A., Kennea, J. A., Dichiara, S., et al. 2023, ApJL, 946, L24
Williamson, M., Modjaz, M., & Bianco, F. 2019, ApJL, 880, 22
Willingale, R., Starling, R. L. C., Beardmore, A. P., Tanvir, N. R., & O'Brien, P. T. 2013, MNRAS, 431, 394
Wilms, J., Allen, A., & McCray, R. 2000, ApJ, 542, 914
Woosley, S. E., & Bloom, J. S. 2006, ARA&A, 44, 507
Yang, J., Ai, S., Zhang, B.-B., et al. 2022, Natur, 612, 232
Yang, S., & Sollerman, J. 2023, ApJS, 269, 40
Yang, Y.-H., Troja, E., O'Connor, B., et al. 2023, arXiv:2308.00638
Zackay, B., Ofek, E. O., & Gal-Yam, A. 2016, ApJ, 830, 27
Zhang, B., & Mészáros, P. 2001, ApJ, 559, 110
Zhang, Z.-D., Yu, Y.-W., & Liu, L.-D. 2022, ApJ, 936, 54
Zheng, W., Filippenko, A. V. & KAIT GRB team 2023, GCN, 34395, 1